NEW ADVANCES

IN

THREE DIMENSIONAL TRANSIENT ELECTROMAGNETIC INVERSION

GREGORY A. NEWMAN*

LAWRENCE BERKELEY NATIONAL LABORATORY

EARTH SCIENCE DIVISION

MS 90-1116

1 CYCLOTRON ROAD

BERKELEY CA 94720

MICHAEL COMMER

INSTITUTE FOR GEOPHYSICS AND METEOROLOGY

UNIVERSITY OF COLOGNE

COLOGNE GERMANY

JUNE 16, 2004

* Formally affiliated with Sandia National Laboratories, Albuquerque New Mexico.

ABSTRACT

Inversion of transient electromagnetic (TEM) data sets to image the subsurface three-dimensional (3-D) electrical conductivity and magnetic permeability properties can be done directly in the time domain. The technique, first introduced by Wang et al. (1994) for causal and diffusive electromagnetic fields and subsequently implemented by Zhdanov and Portniaguine (1997) in the framework of iterative migration, is based upon imaging methods originally developed for seismic wavefields (Claerbout, 1971; Tarantola, 1984). In this paper we advance the original derivations of Wang et al. (1994) and Zhdanov and Portniaguine (1997) to treat non-causal TEM fields, as well as correct a flaw in the theory for treatment of magnetic field data. Our 3D imaging scheme is based on a conjugate-gradient search for the minimum of an error functional involving EM measurements governed by Maxwell's equations without displacement currents. Treatment for magnetic field, voltage (time derivative of the magnetic field) and electric field data are given. The functional can be computed by propagating the data errors back into the model in reverse time along with a DC field, sourced by the integrated data errors over the measurement time range. By correlating these fields, including the time-integrated back-propagated fields, with the corresponding incident field and its initial value at each image point, efficient computational forms for the gradients are developed. The forms of the gradients allow for additional efficiencies when voltage and electric field data are inverted. In such instances the combined data errors can be back-propagated jointly, significantly reducing the computation time required to solve the inverse problem. The inversion algorithm is applied to the long offset transient electromagnetic measurement (LOTEM) configuration thereby demonstrating its capability in inverting

non-causal field measurements of electric field and voltage, sourced by a grounded wire, over complex structures. Findings also show that migration, without iteration or preconditioning, is not an effective imaging strategy; reconstructions at the first inversion iteration bear little resemblance to simple or complex test models.

INTRODUCTION

The time-domain, or transient electromagnetic (TEM) method has shown great potential in hydrological and hazardous waste site characterization (cf., Pellerin and Alumbaugh, 1997), mineral exploration (cf. Nabighian and Macnae, 1991) and general geological mapping and geophysical reconnaissance. Since the technique is designed to map variations in the subsurface electrical conductivity, it is also sensitive to fluid saturation and porosity and permeability changes, thus making the method potentially useful for remotely mapping the fluid properties of hydrocarbon and geothermal reservoirs. Nabighian and Macnae (1991) describes modern TEM systems, which can be deployed using many different types of transmitters and receiver configurations, and can employ various types of transmitter current waveforms. Whatever the configuration of the TEM system, the measurement records the Earth's broadband EM response over a specified time range, in the diffusive regime for EM fields. Thus displacement currents can be neglected, given the bandwidth of the system and scale and measurement times. Here the EM response is sensitive to the conductivity and magnetic permeability properties of the Earth.

Figure 1 illustrates the measurement technique, where the Earth's TEM response due to a loop or wire source is measured at a given location near the Earth's surface or in

a borehole. This measurement can include the magnetic field, or its time derivative (voltage) or electric field at one or more points at fixed distances from the source. The source is then moved to a new location along a survey line or borehole and the sequence is repeated. Such TEM surveys can generate large amounts of data. Hence computational efficiency is essential with any data interpretation scheme.

A very popular and efficient approach to interpret TEM data is one-dimensional (1D) imaging (cf., Macnae and Lamontagne, 1987; Nekut, 1987; Eaton and Hohmann, 1989; Fullagar, 1989; Macnae et al., 1991). Theses types of imaging algorithms generate a conductivity-versus-depth profile at each location along a survey line and are often plotted together to form a two-dimensional (2D) image. To model TEM data arising from magnetic permeability anomalies, Zhdanov and Pavlov (2001) have developed a scheme based upon thin sheet approximations. In general there is scarcity of data interpretation schemes for the electrical parameter μ because spatial variations in magnetic permeability from that of free space are quite rare. When changes in μ do occur, it is associated with magnetic ore bodies and a small number of soils that exhibit high magnetic losses.

It is well known that one-dimensional conductivity imaging schemes allow for fast interpretation of data, but can contain artifacts when applied to data arising from 2D or three-dimensional (3D) geology (cf. Newman et al., 1987). Moreover in other types of TEM measurement systems, such as the long offset transient electromagnetic (LOTEM) method, simple imaging methods are not appropriate and the full dimensionality of the interpretation problem needs to be addressed (cf., Gunderson et al., 1986; Hördt et al., 1992; Hördt, 1998; Hördt and Müller, 2000; Hördt et al., 2000; Commer, 2004).

Recently Zhdanov et al. (2002) introduced an adaptation of the thin sheet method to invert TEM data acquired over inhomogeneous 3D geological structures. While this method looks promising, much work remains to be done in accessing different types of 3D TEM inversion schemes because practical multidimensional TEM inversion and new 3D imaging schemes are now just beginning to emerge (cf., Haber and Oldenburg, 2002). Nevertheless, about twenty years ago, the pioneering work of Zhdanov and Frenkel (1983) (plus many other later works of Zhdanov) have advanced the idea of back propagating or migrating the scattered EM field into the Earth in order to image the source of the scattering. The image condition was based on an analogy to seismic migration (Claerbout, 1971). It was along these lines Wang et al. (1994) developed the theory for solving the full non-linear 3D TEM inverse problem using the concept of back-propagation, in a manner similar to that introduced by Tarantola (1984) for seismic wavefields. Wang et al. significant contribution was the development of efficient computational forms for the cost functional gradients, which are employed in conjugate gradient/steepest descent solutions to the non-linear inverse problem. Gradient type solutions are preferred for treating large-scale data sets involving fine model parameterizations of the imaging domain in order to accurately map complex 3D geological structure. Following up on this work, Zhdanov and Portniaguine (1997) demonstrated that solution of 3D TEM inverse problem could be formulated using iterative migration to derive gradients, which can be used to minimize the residual-field energy flow through the surface or profile of observations. This approach, which employs back-propagation of the residual-field energy flow, is also summarized in Zhdanov's

(2002) book on Geophysical inverse theory, where both the time and frequency domain problems are treated.

While the above-mentioned works comprise much progress in proposing a tractable approach to 3D TEM inversion, we have come to realize that additional work on the problem remains. First, Wang et al. applied their technique to 2D synthetic examples that involved the solution of the scalar wave equation for electric field, and left out crucial details for implementing the technique for general 3D imaging involving vector fields. Moreover their treatment of the gradients was not correctly formulated for magnetic field data types; this problem was not addressed by Zhdanov and Portniaguine (1997) and Zhdanov (2002) treatment of the 3D TEM inverse problem. We will show that the conductivity gradients for magnetic field data actually involve a back-propagated or migrated electric field step response. Second, Wang et al. only considered gradients arising only from causal source fields. Such fields and associated time-derivatives are zero before a given fixed time, typically denoted as time zero and hence cannot be used to treat data arising from a non-causal source. LOTEM would be an example of such a measurement, where static DC electric and magnetic fields are present before the steady transmitter current is shutoff. In contrast Zhdanov's work did treat this problem, but the computational forms of the gradients are cumbersome to implement and not practical as they involve an integration of the migrated field over an indefinite time range, from the latest measurement time, T, to $-\infty$. While this integration can be carried out backwards in time to a point where the migrated field has effectively decayed to zero, it is expensive. In this paper we present new gradient derivations for the non-causal problem that avoids integrating the migrated field before time $t=0$.

Utilizing new gradients, which are specified below, we will formulate a 3D TEM imaging scheme based on the concepts of back-propagation and non-linear conjugate gradient (NLCG) inversion. To make the scheme practical for 3D imaging we will also discuss the details needed for efficient back-propagation and implementation on massively parallel computing architectures and platforms. We will then demonstrate the scheme on LOTEM exploration problems, where a non-causal 3D imaging capability is necessary to interpret the data.

FORMULATION OF THE TEM INVERSE PROBLEM

Error Functional Specification

Consider the following TEM experiment: An EM source (loop or grounded wire), denoted by $\mathbf{s}_j$, is energized with a source waveform *S(t)*, and the transient magnetic field, its time derivative (voltage) and electric field are measured at positions $\mathbf{r}_i \subset \{ \mathbf{r}_1, \ldots, \mathbf{r}_N \}$ from time *t=0* to time *t=T*; before the onset of any measurement the only assumption we make is that the electric and magnetic fields arising from the source are at steady state, and their associated time derivatives are zero everywhere. Let us denote these respective measurements as $\mathbf{h}^o(\mathbf{r}_i, t \mid \mathbf{s}_j)$, $\mathbf{u}^o(\mathbf{r}_i, t \mid \mathbf{s}_j)$ and $\mathbf{e}^o(\mathbf{r}_i, t \mid \mathbf{s}_j)$.

We now seek to find a model (a conductivity distribution $\sigma(\mathbf{r}')$ and a magnetic permeability distribution $\mu(\mathbf{r}')$ such that the transient magnetic field $\mathbf{h}(\mathbf{r}_i, t \mid \mathbf{s}_j)$, the voltage ($\mathbf{u}(\mathbf{r}_i, t \mid \mathbf{s}_j) = -\mu_{coil}\, \partial \mathbf{h}(\mathbf{r}_i, t \mid \mathbf{s}_j) / \partial t$, where μ_{coil} is the magnetic permeability of the detector) or the electric field $\mathbf{e}(\mathbf{r}_i, t \mid \mathbf{s}_j)$, calculated from the model matches the measured field according to some criteria. Here we denote $\mathbf{r}'$ as a point in the region where the model is allowed to vary, and $\mathbf{r}$ denotes a point in the region where

measurements are made. An obvious choice is to match the data in a least squares sense, which corresponds to finding a model that minimizes the error functional,

$$\vartheta(\sigma,\mu)=\frac{1}{2}\sum_{j}\ \sum_{i}\int_{0}^{T}\frac{dt}{t}\ \delta\mathbf{d}^{o}(\mathbf{r}_{i},t\,|\,\mathbf{s}_{j})\cdot\delta\mathbf{d}^{o}(\mathbf{r}_{i},t\,|\,\mathbf{s}_{j})\ . \tag{1}$$

where

$$\delta\mathbf{d}^{o}(\mathbf{r}_{i},t\,|\,\mathbf{s}_{j})=\mathbf{d}^{o}(\mathbf{r}_{i},t\,|\,\mathbf{s}_{j})-\mathbf{d}(\mathbf{r}_{i},t\,|\,\mathbf{s}_{j})\,. \tag{2}$$

Here, $\mathbf{d}^{o}(\mathbf{r}_{i},t\,|\,\mathbf{s}_{j})$ and $\mathbf{d}(\mathbf{r}_{i},t\,|\,\mathbf{s}_{j})$ correspond to the observed and predicted data, be it the magnetic field, voltage or electric field. The dependence of the functional, $\vartheta(\sigma,\mu)$, on the model comes from the implicit dependence of the calculated model response $\mathbf{d}$ on σ and μ, which in turn satisfied the first-order Maxwell's equations in the diffusive approximation (i.e., without displacement currents):

$$\sigma\,\mathbf{e}-\nabla\mathrm{x}\mathbf{h}=-\mathbf{j}_{j} \tag{3}$$

$$\nabla\mathrm{x}\mathbf{e}+\mu\,\partial\mathbf{h}/\partial t=-\mathbf{m}_{j}\,, \tag{4}$$

where $\mathbf{j}_{j}$ denotes electric and $\mathbf{m}_{j}$ magnetic source currents that correspond to $\mathbf{s}_{j}$.

Following Wang et al. (1994) we also introduced a weighting of $\frac{1}{t}$ into the error functional to compensate for different information density at different stages of the transient. This weighting is also equivalent to integrating over logarithmic time in equation (1). For statistical reasons, it is advisable to also weight each field datum with the associated measurement error to prevent undue importance being given to poorly estimated data. In this respect we would weight the components of the data error vector,

$\delta\mathbf{d}^{o}(\mathbf{r}_i, t; \mathbf{s}_j)$, by an estimate of the noise for each component, at that measurement location and time. Nevertheless, where the transient changes sign we still need to exercise caution with this weighting scheme. If too much weight is given to small magnitude data near crossovers the corresponding data fits will be superior, but poorer elsewhere. This phenomenon arises because we are in effect giving too much weight to small magnitude data near the crossover. Hence special care is needed to down weight the data near crossovers. Wang et al. (1994) propose another type of weighting scheme based upon a stitched log transformation of the data with a linear scale for amplitudes near zero. We tested this weighting scheme, but found it not to be that effective compared to the scheme previously described.

To avoid over fitting the data in the presence of noise we find it advantageous to normalize equation (1) by a sum of natural logarithms, whose arguments correspond to the ratio of the latest to earliest delay time for each source-receiver pair. Specifically,

$$\vartheta_N(\sigma,\mu) = \frac{\vartheta(\sigma,\mu)}{\frac{1}{2}\sum_j \sum_i \ln(t_{ji}^{\max}) - \ln(t_{ji}^{\min})}. \qquad (5)$$

We note that the earliest measurable delay time is never zero in equation (5). As the data are fit to the estimated noise level, the normalized component of the error functional (related to the data error) will approach unity, assuming that the data error is Gaussian and normally distributed.

Because we are interested in modeling complex geology it is necessary to impose a fine model parameterization in the inverse solution. This results in many more model parameters than data values, and further compounds the instability of the TEM

inverse solution. The stabilization approach adopted here uses Tikhonov regularization (Tikhonov and Arsennin, 1977), which imposes a smoothness constraint on the variation of the Earth's electrical conductivity and magnetic permeability properties, and comes at an expense of an increase in the data error, $\delta\mathbf{d}^{\circ}$, at the final model. To implement the regularization, we divide the earth into M cells and assign to each cell an initial electrical conductivity and a magnetic permeability value. Let a model vector, **m**, which is of length 2M, denote these geo-electrical properties and augment the error functional (equation (1)) such that

$$\vartheta(\sigma,\mu)=\frac{1}{2}\sum_{j}\sum_{i}\int_{0}^{T}\frac{dt}{t}\;\delta\mathbf{d}^{\circ}(\mathbf{r}_i,t;\mathbf{s}_j)\cdot\delta\mathbf{d}^{\circ}(\mathbf{r}_i,t;\mathbf{s}_j)+\frac{\lambda}{2}\mathbf{m}^{\mathbf{T}}\mathbf{W}^{\mathbf{T}}\mathbf{W}\mathbf{m}\,. \qquad (6)$$

The regularization matrix, $\mathbf{W}$, consists of a finite-difference approximation to the Laplacian (∇^2) operator and the tradeoff parameter, λ, dictates the amount of smoothing to be incorporated into the model and **T** denote the transpose operator. It is now understood that we seek solutions to Maxwell's equations (equations (3) and (4)), where σ and μ are piece-wise constant.

Newman and Alumbaugh (2000) point out that the tradeoff parameter should be held fixed during inversion iteration. To vary it would, in principal, invalidate the use of previous search directions in the NLCG iteration. The common recipe in selecting λ is based upon a cooling approach (cf., Haber and Oldenburg, 1997); we carry out multiple solutions to the inverse problem using non-linear conjugate gradients, starting with large fixed value for λ. As λ is reduced, the data error, represented by the first term in equation (6) will decrease. We continue this process of reducing λ, until the data error agrees with a target misfit based upon the assumed noise content of the data. Note that if

λ is to be changed during the NLCG iteration, it will be necessary to discard the previous search direction, and re-initialize the algorithm using the steepest descent direction at the current model.

As previously mentioned minimization of equation (6) is to be carried out using the method non-linear conjugate gradients. This method is ideal for treating extremely large data sets and imaging volumes because of its minimal storage and computational requirements and converges faster than steepest descent (cf. Wang et al., 1994; Newman and Alumbaugh, 2000; Zhdanov 2002). With a careful implementation of non-linear conjugate gradient scheme, each inversion iteration requires only a few solutions of the forward modeling problem for each fixed source, and also includes the initial value or DC related problem for non-causal fields. Specifically, one application of the forward code is used to compute the data in the current model, another to compute the gradient, and one or two additional simulations to compute a step length along a descent direction.

Specification of the Gradients

Efficient computation of the gradient of the error functional is critical in a non-linear conjugate gradient scheme. To fully understand how we will arrive at computationally efficient gradients, refer to Appendix A for a brief review on the theory of Maxwell's equations for 3D heterogeneous media, solution of these equations using dyadic Green's functions and their corresponding adjoints. A short discussion on the reciprocity relationships between dyadic Green's functions and their adjoints will also be presented. This review will provide the necessary background to develop efficient

formulas for the error functional gradient, extended to non-causal field sourcing for electric field, voltage and magnetic field data types. It will also allow us to show that the conductivity gradients for magnetic field data actually involve a back-propagated electric field step response.

In the table below we state the formulas for the gradients of electric field data, γ_σ^e and γ_μ^e, voltage, γ_σ^u and γ_μ^u, and magnetic field, γ_σ^h, and γ_μ^h; detailed derivation of these gradients can be found in Appendices B, C and D. Note further that these gradients treat only the data component of the error functional (equation (1)) and are considered differential or point gradients; there is no volume associated with the point where the gradient is evaluated. To obtain gradients with respect to a finite size volume or cell, they must be integrated over the volume of that cell; here we multiply the point gradients at the cell center by the corresponding cell volume and add to them the regularized component of the gradient, determined directly from the second term equation (6), where

$$\gamma^{reg} = \lambda \mathbf{W}^{\mathbf{T}}\mathbf{W}\mathbf{m}. \qquad (7)$$

In a later section of the paper we will discuss how the cell-based gradients are further stabilized to provide positive estimates of the piece wise constant electric parameters, σ and μ..

Point Wise Gradients for Electric Conductivity

$$\gamma_{\sigma}^{e}(\mathbf{r}') = \sum_{j} \int_{0}^{T} dt' \, \mathbf{e}(\mathbf{r}', t'; \mathbf{s}_j) \cdot \mathbf{e}_b(\mathbf{r}', t'; \mathbf{s}_j \mid \delta\mathbf{e}^o)$$

$$- \sum_{j} \mathbf{e}_{DC}(\mathbf{r}'; \mathbf{s}_j) \cdot \int_{0}^{T} dt' \mathbf{e}_b(\mathbf{r}', t'; \mathbf{s}_j \mid \delta\mathbf{e}^o) + \sum_{j} \mathbf{e}_{DC}(\mathbf{r}'; \mathbf{s}_j) \cdot \mathbf{e}_b^{DC}(\mathbf{r}'; \mathbf{s}_j \mid \delta\mathbf{e}^o).$$

$$\gamma_{\sigma}^{u}(\mathbf{r}') = \sum_{j} \int_{0}^{T} dt' \mathbf{e}(\mathbf{r}', t'; \mathbf{s}_j) \cdot \mathbf{e}_b(\mathbf{r}', t'; \mathbf{s}_j \mid \delta\mathbf{u}^o)$$

$$- \sum_{j} \mathbf{e}_{DC}(\mathbf{r}'; \mathbf{s}_j) \cdot \int_{0}^{T} dt' \mathbf{e}_b(\mathbf{r}', t'; \mathbf{s}_j \mid \delta\mathbf{u}^o)$$

$$\gamma_{\sigma}^{h}(\mathbf{r}') = \sum_{j} \int_{0}^{T} dt' \, \mathbf{e}(\mathbf{r}', t'; \mathbf{s}_j) \cdot \mathbf{e}_b^{step}(\mathbf{r}', t'; \mathbf{s}_j \mid \delta\mathbf{h}^o)$$

$$- \sum_{j} \mathbf{e}_{DC}(\mathbf{r}'; \mathbf{s}_j) \cdot \int_{0}^{T} dt' \, \mathbf{e}_b^{step}(\mathbf{r}', t'; \mathbf{s}_j \mid \delta\mathbf{h}^o) + \sum_{j} \mathbf{e}_{DC}(\mathbf{r}'; \mathbf{s}_j) \cdot \mathbf{e}_b^{DC}(\mathbf{r}'; \mathbf{s}_j \mid \delta\mathbf{h}^o)$$

Point Wise Gradients for Magnetic Permeability

$$\gamma_{\mu}^{e}(\mathbf{r}') = \sum_{j} \int_{0}^{T} dt' \, \frac{\partial}{\partial t'} \mathbf{h}(\mathbf{r}', t'; \mathbf{s}_j) \cdot \frac{\partial}{\partial t'} \mathbf{h}_b(\mathbf{r}', t'; \mathbf{s}_j \mid \delta\mathbf{e}^o)$$

$$\gamma_{\mu}^{u}(\mathbf{r}') = \sum_{j} \int_{0}^{T} dt' \, \frac{\partial}{\partial t'} \mathbf{h}(\mathbf{r}', t'; \mathbf{s}_j) \cdot \frac{\partial}{\partial t'} \mathbf{h}_b(\mathbf{r}', t'; \mathbf{s}_j \mid \delta\mathbf{u}^o)$$

$$\gamma_{\mu}^{h}(\mathbf{r}') = \sum_{j} \int_{0}^{T} dt' \, \frac{\partial \mathbf{h}(\mathbf{r}', t'; \mathbf{s}_j)}{\partial t'} \cdot \mathbf{h}_b(\mathbf{r}', t'; \mathbf{s}_j \mid \delta\mathbf{h}^o) + \sum_{j} \mathbf{h}_{DC}(\mathbf{r}'; \mathbf{s}_j) \cdot \mathbf{h}_b^{DC}(\mathbf{r}'; \mathbf{s}_j \mid \delta\mathbf{h}^o)$$

Table 1.

Fields for the forward problem, including their initial values at DC, are specified by $\mathbf{e}$ and $\mathbf{e}_{DC}$ for the electric field and $\mathbf{h}$ and $\mathbf{h}_{DC}$ for the magnetic field. The time dependent fields, $\mathbf{e}$ and $\mathbf{h}$, satisfies Maxwell's equations (3) and (4), while the DC fields are determined by solving these equations in the steady state limit. It is reasonable to

define different types of back-propagated fields, as becomes clear from the gradient derivations in the appendices. First one has to distinguish between data residuals/errors as defined by equation (2) because the conductivity gradient will depend upon data type. These gradients involve a back-propagated electric field, denoted by $\mathbf{e}_b$, which can be sourced by data residuals/errors in the electric field, voltage or magnetic field. However, for magnetic field data, the back-propagated electric field step response of $\mathbf{e}_b$ is actually required and is given by, $\mathbf{e}_b^{step}(\mathbf{r}',t';\mathbf{s}_j \mid \delta\mathbf{h}^o) = \int_T^{t'} dt\, \mathbf{e}_b(\mathbf{r}',t;\mathbf{s}_j \mid \delta\mathbf{h}^o)$. To treat the non-causal part of the conductivity gradients (γ_σ^e and γ_σ^h) we require DC back propagated electric fields, $\mathbf{e}_b^{DC}(\mathbf{r}';\mathbf{s}_j \mid \delta\mathbf{e}^o) = \int_{-\infty}^{T} dt\, \mathbf{e}_b(\mathbf{r}',t;\mathbf{s}_j \mid \delta\mathbf{e}^o)$ and $\mathbf{e}_b^{DC}(\mathbf{r}';\mathbf{s}_j \mid \delta\mathbf{h}^o) = \int_{-\infty}^{T} dt\, \mathbf{e}_b(\mathbf{r}',t;\mathbf{s}_j \mid \delta\mathbf{h}^o)$, which are sourced by the electric and magnetic field data errors, and satisfy the back-propagation field equations at steady state. A back-propagated magnetic field is needed to specify gradients for the magnetic permeability, where $\mathbf{h}_b$ can be sourced for electric field, voltage and magnetic field data errors; for electric field and voltage data we actually require the time derivative of $\mathbf{h}_b$. To complete the specification, a DC back-propagated magnetic field, $\mathbf{h}_b^{DC}(\mathbf{r}';\mathbf{s}_j \mid \delta\mathbf{h}^o)$, sourced by the magnetic field data errors is also required for γ_μ^h.

From Wang et al. (1994) one can show that the back-propagated fields $\mathbf{e}_b$ and $\mathbf{h}_b$, sourced with the electric field data errors $\delta\mathbf{e}^o$ at all the receiver positions radiating as electrical current sources in reverse time satisfy the adjoint Maxwell equations that are given by

$$\sigma \mathbf{e}_b + \nabla \mathrm{x} \mathbf{h}_b = -\sum_i \frac{\delta \mathbf{e}^o(\mathbf{r}_i, t; \mathbf{s}_j)}{t} \delta(\mathbf{r} - \mathbf{r}_i) \tag{8}$$

$$\nabla \mathrm{x} \mathbf{e}_b + \mu \partial \mathbf{h}_b / \partial t = 0 \tag{9}$$

from time $t = T$ to 0, where $\mathbf{e}_b$ and $\mathbf{h}_b$ are zero for $t \geq T$. Similar equations and final conditions hold for the back-propagated fields sourced by either the voltage or magnetic field data residuals. For the voltage residuals, the back-propagation field equations are given as

$$\sigma \mathbf{e}_b + \nabla \mathrm{x} \mathbf{h}_b = 0 \tag{10}$$

$$-\nabla \mathrm{x} \mathbf{e}_b - \mu \partial \mathbf{h}_b / \partial t = -\sum_i \mu(\mathbf{r}_i) \frac{\delta \mathbf{u}^o(\mathbf{r}_i, t; \mathbf{s}_j)}{t} \delta(\mathbf{r} - \mathbf{r}_i), \tag{11}$$

while for magnetic field data residuals, they are

$$\sigma \mathbf{e}_b + \nabla \mathrm{x} \mathbf{h}_b = 0 \tag{12}$$

$$-\nabla \mathrm{x} \mathbf{e}_b - \mu \partial \mathbf{h}_b / \partial t = -\sum_i \frac{\delta \mathbf{h}^o(\mathbf{r}_i, t; \mathbf{s}_j)}{t} \delta(\mathbf{r} - \mathbf{r}_i). \tag{13}$$

over the time range $t = T$ to 0.

Derivation of the back-propagated DC field equations for $\mathbf{e}_b^{DC}$ and $\mathbf{h}_b^{DC}$ sourced by the electric and magnetic field data errors can also be found in Appendix B and D, respectively. Here we state the equations directly. For $\mathbf{e}_b^{DC}$ sourced by the magnetic field data errors, we have

$$\nabla \mathrm{x} \nabla \mathrm{x} \mathbf{e}_b^{DC} = \nabla \mathrm{x} \sum_i \int_0^T dt \frac{\delta \mathbf{h}^o(\mathbf{r}_i, t)}{t} \delta(\mathbf{r} - \mathbf{r}_i). \tag{14}$$

Because equation (14) has a nontrivial null space (the vector fields described by the gradient of a scalar potential), special techniques are needed to deflate this null space out from $\mathbf{e}_b^{DC}(\mathbf{r}'|\delta\mathbf{h}^o)$. Methods of solution that accomplish this task can be found in Chan et al. (2002). For $\mathbf{e}_b^{DC}$, sourced by the electric field data errors, we set $\nabla\theta_b = \mathbf{e}_b^{DC}$ and solve the following Possion problem

$$\nabla\cdot\sigma\nabla\theta_b = -\nabla\cdot\sum_i\int_0^T dt\ \frac{\delta\mathbf{e}^o(\mathbf{r}_i,t;\mathbf{s}_j)}{t}\,\delta(\mathbf{r}-\mathbf{r}_i)\,. \tag{15}$$

Analogously for $\mathbf{h}_b^{DC}$ we set $\nabla\phi_b = \mathbf{h}_b^{DC}$ and solve

$$\nabla\cdot\mu\nabla\phi_b = \nabla\cdot\sum_i\int_0^T dt\ \frac{\delta\mathbf{h}^o(\mathbf{r}_i,t;\mathbf{s}_j)}{t}\,\delta(\mathbf{r}-\mathbf{r}_i)\,, \tag{16}$$

for the back-propagated DC magnetic field problem.

Thus, the gradients for a fixed source can be computed by propagating the data errors back into the model in reverse time along with a DC field that arises with the time integrated electric or magnetic field data errors. By correlating these fields, including the time-integrated back-propagated fields, with the corresponding incident field and its initial value at each image point, efficient computational forms for the gradients have been developed. Moreover, with a given source and data type, as Wang et al., (1994) demonstrated, two forward simulations are required using Maxwell equations (3)-(4) forward in time and the corresponding adjoint equations backwards in time, equations (8)-(9), (10)-(11), or (12)-(13). While these adjoint equations depend upon the data type, they can be stepped backward in time with exactly the same finite difference algorithm that marches the ordinary Maxwell's equations forward in time (Commer and Newman, 2004; Wang et al., 1994). However, if a static field is present before the

transmitter/source is shutoff, we also have two additional DC boundary value problems to solve. The first gives the DC field in the medium due to the impressed source and the second the back-propagated DC field, which is sourced with the time-integrated electric or magnetic field data errors (equations (14), (15) or (16)).

From these tables we observe that the gradient for electric field and voltage data types can be computed jointly if both types of data are present; this allows for additional efficiencies when voltage and electric field data are jointly inverted. Using superposition, the combined electric conductivity and magnetic permeability gradients are specified as

$$\begin{aligned}\gamma_{\sigma}^{e+v}(\mathbf{r}') = \sum_j & \int_0^T \mathbf{e}(\mathbf{r}',t';\mathbf{s}_j)\cdot\mathbf{e}_b(\mathbf{r}',t';\mathbf{s}_j \mid \delta\mathbf{e}^o + \delta\mathbf{u}^o)dt' \\ & - \sum_j \mathbf{e}_{DC}(\mathbf{r}';\mathbf{s}_j)\cdot\int_0^T \mathbf{e}_b(\mathbf{r}',t';\mathbf{s}_j \mid \delta\mathbf{e}^o + \delta\mathbf{u}^o)dt \\ & + \sum_j \mathbf{e}_{DC}(\mathbf{r}';\mathbf{s}_j)\cdot\mathbf{e}_b^{DC}(\mathbf{r}';\mathbf{s}_j \mid \delta\mathbf{e}^o)\end{aligned} \tag{17}$$

and

$$\gamma_{\mu}^{e+v}(\mathbf{r}') = \sum_j \int_0^T dt' \frac{\partial}{\partial t'}\mathbf{h}(\mathbf{r}',t';\mathbf{s}_j)\cdot\frac{\partial}{\partial t'}\mathbf{h}_b(\mathbf{r}',t';\mathbf{s}_j \mid \delta\mathbf{e}^o + \delta\mathbf{u}^o), \tag{18}$$

where the combined back-propagated fields can be obtained from

$$\sigma\mathbf{e}_b + \nabla\mathrm{x}\mathbf{h}_b = -\sum_i \frac{\delta\mathbf{e}^o(\mathbf{r}_i,t;\mathbf{s}_j)}{t}\delta(\mathbf{r}-\mathbf{r}_i) \tag{19}$$

$$\nabla\mathrm{x}\mathbf{e}_b + \mu\,\partial\mathbf{h}_b/\partial t = -\sum_i \mu(\mathbf{r}_i)\frac{\delta\mathbf{u}^o(\mathbf{r}_i,t;\mathbf{s}_j)}{t}\delta(\mathbf{r}-\mathbf{r}_i) \tag{20}$$

over the time range $t = T$ to 0. Back-propagating the combined data errors (electric field and voltage) for a fixed source significantly reduces the time required to compute the

gradients and ultimately impacts on the time needed to solve the TEM inverse problem. This result also differs with derivations found in Zhdanov (2002) and Zhdanov and Portniaguine (1997) where joint migration or back-propagation of the data residuals involves electric and magnetic fields, instead of electric fields and voltages. In our derivations it is not possible to use back-propagated fields, jointly sourced by electric and magnetic field data residuals, to more efficiently compute the gradients.

Back-Propagation

To clarify how back-propagation is accomplished in this paper, we first specify some details on the explicit finite difference time domain (FDTD) scheme used in the forward modeling problem. From Wang and Hohmann (1993), electric and magnetic fields arising from electric sourcing for example, are in effect advanced with the following equations:

$$\mathbf{h}(\mathbf{r})^{n+1/2} = \mathbf{h}(\mathbf{r})^{n-1/2} - \frac{\Delta t_n}{\mu(\mathbf{r})} \nabla \mathrm{x} \mathbf{e}(\mathbf{r})^n \tag{21}$$

and

$$\mathbf{e}(\mathbf{r})^{n+1} = \left(\frac{2\gamma - \sigma \Delta t_n}{2\gamma + \sigma \Delta t_n} \right) \mathbf{e}(\mathbf{r})^n + \left(\frac{2\Delta t_n}{2\gamma + \sigma \Delta t_n} \right) \{ \nabla \mathrm{x} \mathbf{h}(\mathbf{r})^{n+1/2} - \mathbf{j}(\mathbf{r})^{n+1/2} \} . \tag{22}$$

Here Δt_n denotes the variable time step taken at time t_n, where equation (21) advances the magnetic field ($\mathbf{h}^{n+1/2}$) to time $t_{n+1/2}$ and equation (22) advances the electric field ($\mathbf{e}^{n+1}$) to time t_{n+1}. The variable γ is a fictitious displacement current term. It is much larger than the true displacement current, but still small enough to allow accurate simulation of Maxwell's equations in the diffusive approximation. Its incorporation allows for the use of larger time steps than with a conventional Euler type scheme applied directly to

equations (3) and (4) (see Wang and Hohmann (1993) or Chew (1990) for details). As the fields are advanced, we also increase the size of the time step in equations (21) and (22), reducing the computation time required for field simulation at later times. A simple formula provided by Wang and Hohmann (1993) can be used to determine the size of the time step, where we first need to specify the minimum conductivity and permeability encountered in the modeling problem, along with the time, t_n, where

$$\Delta t_n \sim \sqrt{\frac{\mu_{\min}\sigma_{\min}\, t_n}{6}}\,. \tag{23}$$

Equation (23) is designed to preserve the diffusive nature of the fields; while larger time steps can be taken, since the time stepping scheme is unconditionally stable, the fields can be affected adversely by the fictitious displacement current term, displaying erroneous wave-like properties.

We have already indicated that we use the same FDTD scheme for back-propagation, because the stability properties of the two operations, forward- and back-propagation, are the same. Hence the back-propagated fields in equations (12) and (13), for example, can be decremented from

$$\mathbf{h}_b(\mathbf{r})^{n-1/2} = \mathbf{h}_b(\mathbf{r})^{n+1/2} + \frac{\Delta t_n}{\mu(\mathbf{r})}\nabla \mathrm{X}\mathbf{e}_b(\mathbf{r})^n - \frac{\Delta t_n}{\mu(\mathbf{r})}\sum_i \left(\frac{\delta\mathbf{h}(\mathbf{r}_i)^{o\,n+1/2} + \delta\mathbf{h}(\mathbf{r}_i)^{o\,n-1/2}}{2} \right)\delta(\mathbf{r}-\mathbf{r}_i) \tag{24}$$

and

$$\mathbf{e}_b(\mathbf{r})^n = \left(\frac{2\gamma - \sigma\Delta t_n}{2\gamma + \sigma\Delta t_n}\right)\mathbf{e}_b(\mathbf{r})^{n+1} - \left(\frac{2\Delta t_n}{2\gamma + \sigma\Delta t_n}\right)\nabla \mathrm{X}\mathbf{h}_b(\mathbf{r})^{n+1/2}\,. \tag{25}$$

In computing the back-propagated fields with equations (24) and (25), the fields are initialized to zero at $t=T$, and the fields are computed backwards from the point, where

the data differences are fed in as source terms at the receiver locations (starting with the values at time *T*). As the fields are back-propagated, the variable time step is decreased. The initial time step used in back-propagation is calculated such that the EM field retains its diffusive nature at the latest observed time and the variable time step decreases, according to equation (23) as the simulation time decreases, until time zero is reached. In carrying out the forward- and back-propagation, the fields are sampled on a staggered grid, where spatial derivatives in equations (21), (22), (24) and (25) are approximated using finite differences (see Commer and Newman (2004) or Wang and Hohmann (1993) for additional details).

Positivity Constraints on the Gradients

An important constraint on electrical conductivity and magnetic permeability is that they must be positive quantities. To enforce this constraint on the inverse solution, we consider a logarithmic transformation, which allows for the incorporation of a lower bounding constraint on conductivity and permeability at each cell. Let us define a new parameter, u_k, at cell *k*. This new parameter is related to the model parameter, m_k, which represents either the conductivity or permeability of the cell by the relation

$$u_k = \ln(m_k - lb_k) \tag{26}$$

or

$$m_k = e^{u_k} + lb_k \tag{27}$$

where lb_k is a lower bounding constraint, such that $m_k > lb_k$. The effect of this log transformation on the corresponding component of the gradient, sensitive to the data

errors, is to scale it by a factor $m_k - lb_k$. Furthermore, the regularized inverse solution will now be designed to produce smooth estimates of the transformed parameters. Nevertheless, experience shows that we can still expect smooth reconstructions of conductivity and permeability properties as well (Newman and Alumbaugh, 1997).

Computation of the Gradients

In the actual computation of gradients, special attention is needed for efficient evaluation of the temporal integrations that are specified in the gradient tables. Hence during the forward simulation, the TEM fields are extracted on a predefined abscissa raster, which is calculated from the Gauss-Legendre N-point quadrature formula, where the number of integration points N is predefined. Selection of N should be optimized according to some criteria which avoids over sampling. On the other hand the sampling must provide for a sufficient number of points to avoid under sampling the fields at the times where rapid variations in the TEM field are to be expected. We have determined that a higher density of abscissa points at early and late times on the raster is somewhat advantageous, since during forward- propagation, rapid variations are observed at early times and during back-propagation stronger variations can be observed at both early and late times. However, these findings are preliminary, and more investigation is needed for further clarification. Thus we have also included the option of storing the forward-propagated fields at all sampled time points employed in the FDTD scheme (time sampling based upon equation (23)). While such field sampling significantly increases the memory needed for storing the forward- propagated fields it can be used to determine an optimal quadrature formula for subsequent production runs. The temporal integration is done during the back- propagation in order to save memory. As soon as a point is

crossed on the predefined abscissa raster, where the forward-propagated field is stored, the back-propagated field is multiplied with the corresponding forward-propagated field and summed up either using the Gauss-Legendre N-point quadrature formula or with a simpler linear quadrature scheme.

Parallel Implementation

Because the computational bottleneck in the 3D TEM inversion scheme is the time required for solving the forward- and back-propagation problems, we have implemented solutions of these problems, including the entire NLCG iteration, on parallel computing architectures. An additional advantage to using parallel computing resources is the ability to simulate greater complexity and realism in the geological modeling of 3D TEM fields, which cannot be achieved using serial machines. Details on the implementation of the parallel 3D FDTD scheme used to forward- and back-propagate the fields can be found in the work of Commer and Newman (2004). Fortunately, parallel implementation of the NLCG iteration introduced above is not difficult. All that is required is global communication amongst the processors to complete dot products, and the step length needed in the line search. To facilitate the parallel implementation of the inversion scheme, we have also written the algorithm in Fortran 90, with dynamic memory allocation, where inter-processor communication is carried out using the Message Passing Interface (MPI) (see Gropp et al., 1999). In addition to the MPI library, we also utilized the AZTEC parallel solver library (Tuminaro et al., 1999) for the solving of the forward- and back-propagated DC field equations.

DEMONSTRATION

Gradient Checks

Gradient checks for electrical conductivity, computed using back-propagation, have been undertaken and are presented here; we have not included checks or inversion test examples for the magnetic permeability as these checks and examples will follow in a subsequent publication. In the gradient checks we consider both magnetic and electric dipole sourcing for a crosswell measurement configuration (Figures 2 and 3). The source (magnetic or electric dipole) is located at x = 0 m, y = 0 m and z = 0 m and only a single receiver (magnetic field, voltage and electric field) located at x = 100 m, y = 0 m and z = 0 m is considered. Note that the gradient at a fixed cell (cell *i*) lying between the transmitter and receiver wells can also be obtained by perturbing equation (6),

$$ {}^{p}\gamma_{\sigma}^{d}(r_i) \approx \frac{\vartheta(\sigma + \Delta\sigma_i, \mu) - \vartheta(\sigma, \mu)}{\Delta\sigma_i} \ , \qquad (28) $$

where d and r_i specify by the data type and cell-center location, respectively. Gradients computed with equation (28) provide a way to check and compare the gradients computed via back-propagation. Here we set λ=0 to focus the comparisons on the component of the gradient represented solely by the data errors. The synthesized observed data used to make the gradient comparisons was created from a 0.2 S/m whole space, where the back-propagation and perturbation calculations assumed a 0.1 S/m medium as the current model. Figures 2 and 3 compare results for the two computational techniques for the gradient as percentage difference plots. In these plots the source waveform is constant until time zero and is then shut off assuming a linear ramp. Note

further that the source waveform is zero after 0.1 μsec and that the data produced from this source were generated over the time range of 10 to 100 μsec. Away from the transmitter and receiver well the comparisons are quite good, within a few percent as illustrated in Figures 2 and 3. However, near the receiver and transmitter wells differences can be as large as fifty percent, but better agreement can be obtained by refining the mesh. Figure 4 demonstrates this claim, where the number of grid nodes in the vicinity of the receiver well has been doubled. Now, in comparison with Figure 2c, the maximum percentage difference in the gradients is reduced by nearly a factor of two from forty seven percent to twenty seven percent. Significant improvement is also observed for all image points along the receiver well.

LOTEM Exploration Problems

a) simple model

The inversion algorithm is now applied to the long offset transient electromagnetic (LOTEM) measurement configuration thereby demonstrating its capability in inverting non-causal field measurements of electric field and voltage, sourced by a grounded wire. The data were generated using a spectral Lanczos scheme (Druskin and Knizhnerman, 1994) for a 1 S/m prismatic body embedded in a 0.1 S/m half-space (Figure 5). The lateral dimensions of the body are 200 m in both the East-West (x direction) and North-South (y direction), where this later direction also corresponds to the orientation of the 80 m long LOTEM transmitter. The body depth extent and depth of burial are 140 m and 60 m, respectively. At the Earth's surface, a receiver grid of 99 detectors is located over the body (Figure 6); the center of the buried body would project

to the coordinate pair (x=300 m, y=0 m) on the receiver grid. The data comprise the y-directed electric field, and vertical voltage, $u_z = -\mu_{coil}\,\partial h_z / \partial t$, over the time range of 0.5 to 70 msec. These data are sampled at 90 delay times and the transmitter waveform is a shut off in a step-wise fashion. We did not add any Gaussian noise to the data. That is not to say that the data are noise free, since numerical noise is present. The numerical noise, which we determined to be about several percent, is quantified by the difference between the synthetic data produced from the two different modeling codes for the exact model.

Because the air is present in the model in Figure 5, new complications arise. In the presence of the air-earth interface, there are some disadvantages with an explicit FDTD scheme used to forward and back-propagate the fields in our inversion scheme. Meshing of the air must be avoided for computational efficiency otherwise extremely small time steps are required to insure stability. In the FDTD scheme this is accomplished by imposing an upward continuation condition on the vertical magnetic fields or their time derivatives at the earth surface (see Commer and Newman, (2004) for details). This upward continuation is actually carried out using a 2D fast Fourier transform (FFT), but has several drawbacks. First is the assumption that the air-earth interface is flat and exhibits no topographic variations. The second is that the 2D FFT does not parallelize as well as other parts of the FDTD solution and this impacts on the overall time efficiency of the algorithm and consequently the corresponding solution efficiency of the inverse problem. Fortunately, one can avoid using the FFT in the forward- and back-propagation of the fields by modeling the air as a finite resistive medium, provided that the medium is not too resistive and the time step required is not too small. Using a time step of 1e-6 seconds, we determined that the air layer present in our model (Figure 5), could be

replaced with an insulating 0.0002 S/m medium, over the time range of the synthetic field measurements (0.5 to 70 msec). Such an approximation also allows one to incorporate topography in the modeling and improves with increasing delay time. However, it can be quite poor at early times. Hence it is essential that the approximation be validated before inverting field data in the presence of an air-earth interface. It is also possible to circumvent these problems by reverting to an implicit type method in the forward- and back- propagation of the fields (Haber and Oldenburg, 2002). Such a scheme has advantages. It allows the use of significantly larger time steps, compared to an explicit scheme and the air can be meshed directly, which also allows for the incorporation of topography in the model. A disadvantage of an implicit scheme, however, is that at every time step a large linear system must be solved and this is time consuming. Future research will determine the optimal solution method for the 3D TEM field simulation in terms of flexibility, speed and robustness.

Using 336 processors on the Sandia National Laboratory ASCII RED machine, we jointly inverted the simulated electric field and voltage data with a two layered starting model, where 0.0002 S/m medium denotes the air, which is fixed in the inversion process, and 0.1 S/m the Earth. The tradeoff parameter was fixed at unity. We also used data weighting based on five percent of the observed measurements at each detector location and delay time, in order to more easily quantify the quality of the data fit. Thus, fitting the normalized data error, (equation (5)) to one implies that we have matched the observations to about 5%, provided the noise present in the data satisfies a Gaussian distribution. Because the actual noise in the data is non-Gaussian, a better measure for quantifying the data fit is to compute equation (5) using the predicted data for the exact

model, which we have also done. After 87 inversion iterations, where each iterate required slightly more than 5 hours, we have decreased the normalized error functional based upon equation (5) (dashed curve) from an initial value of 38 to 0.3 and the corresponding data error measure (solid curve) from 38 to 0.176 (Figure 7). When the exact model is simulated the data error is given as 0.126, which corresponds to fitting the observed data to about five percent, on average. Figure 8 and 9 show the data fits for electric field and voltage for center profile (Y = 0 m) over the target body for six different delay times, ranging from 1 to 50 ms. These figures also show the corresponding data fits after the first inversion iteration, demonstrating the significant improvement in the data fits as the model is iterated.

We have located the body, fairly well (Figures 10 and 11). Moreover the reconstructed conductivity, within the top parts of the imaged body, approaches the true value of 1 S/m. Figures 12 and 13 show the corresponding reconstructions after the first inversion iteration, which also corresponds to the migration of the initial data errors into the model (Zhdanov and Portniaguine, 1997). These images do not indicate the target body, where changes from the half-space starting model are quite modest and seen in the near surface beneath the receiver array, as well as below the transmitter. In this example, migration, without iteration, is not an effective imaging strategy. Wang et al., (1994) observed similar findings for 2D cross-well problems, where rapid decrease in the data misfit at the early inversion iterations produced minor changes in the starting model. Increased model enhancement was seen starting only at the later iterations. However, if the gradients can be suitably preconditioned to allow for a much greater reduction in the

error functional at the first inversion iteration, then migration may provide better results. This point will be discussed in more detail in the concluding section of the paper.

b) complex model

A more complex example is now presented in Figure 14. The model consists of two near surface bodies, one resistive (0.005 S/m) and the over conductive (0.05 S/m), embedded in a 0.01 S/m half-space. A deeper, dipping body (0.1 S/m) is also present. Data for this model was also generated using the spectral Lanczos scheme (Druskin and Knizhnerman, 1994) for the receiver array shown in Figure 15. When the FDTD scheme is used to compute the predicted response of the model, we observed the differences in the calculated responses from the two modeling codes to be within 10 percent, which we denote as the error we will attempt to fit the data too; no additional noise was added to the data. The data comprise the y-directed electric field, and vertical voltage, $\mathrm{u}_z = -\mu_{coil}\,\partial \mathrm{h}_z / \partial t$, over the time range of 0.1 to 10 msec. The 286 detectors shown in Figure 15 are not located on a uniform 2D receiver grid, which is typical with field deployments since some regions of a survey area are often inaccessible for measurements due to a variety of logistical reasons. Note further the refinement in the finite difference mesh over the two near surface structures. Justification for refining the mesh is based on the rapid spatial variation in the observations over the near surface bodies. We have also varied the meshing with depth. It is finest in the near surface, 10 m, but coarsened to 30 m, below 80 m depth, to reflect the reduction in the resolving power of the data with increasing depth. We jointly inverted the simulated electric field and voltage data with a two layered starting model, where 0.0002 S/m medium denotes the air and 0.01 S/m the Earth. The tradeoff parameter again was fixed at unity.

After 65 inversion iterations, where each iterate required slightly more than 8 hours using 336 processors, we have decreased the normalized error functional based upon equation (5) (dashed curve) from an initial value of 10.5 to 0.168 and the corresponding data error measure (solid curve) from 10.5 to 0.115 (Figure 16). When the exact model is simulated the data error is given by 0.137, which implies we are fitting the observed data in the range of the anticipated errors. Figure 17 and 18 show the data fits for electric field and voltage over three selected profiles (Y = 81 m, -12 m, -81 m) for six different delay times, ranging from 0.1 to 10 ms. The voltage data plots at the latest delay time (5 ms) also illustrates some of the noise in the numerically generated observations. The noise was so large that parts of the voltage observations along the data profile were not used in the inversion. This noise behavior in the late time data is also typical of actual TEM field measurements.

The reconstructed images shown in Figures 19 and 20, have clearly located both the near surface resistive and conductive structures. The deeper conductor is also imaged, and its dip is indicated. However, the deeper section of this body is not imaged well, most likely due to a lack of resolving power in the data and conductive shielding from the near-surface conductor. Nevertheless, these reconstructions clearly show the ability of our 3D TEM inversion code to image complex structures. Furthermore, reconstructions after the first inversion iteration do not indicate the three target bodies, where changes from the half-space starting model are minimal. As in the previous example, without iteration or preconditioning, migration is not an effective imaging strategy.

CONCLUSIONS AND SUGGESTIONS FOR FUTURE STUDIES

In this paper, we have presented a new scheme for the inversion of 3D TEM fields with non-causal sourcing. Our scheme employs non-linear conjugate gradient search for minimization of the error functional and the concept of back-propagation, developed from previous works, to efficiently evaluate the gradients. Treatment of electric, magnetic and voltage measurement types has been given. In the course of developing our scheme we have also corrected an error in the original gradient derivations of Wang et al. (1994) for magnetic field data and successfully demonstrated the scheme on 3D exploration problems for the LOTEM measurement configuration. The next logical step will be to demonstrate the 3D inversion scheme on field data.

It is clear that faster solutions to the forward problem as well as more powerful optimization strategies would be beneficial in solving the 3D TEM inverse problem. We adopted a gradient search method for the iterative solution process because it limits the amount of forward modeling overhead, but this comes at the expense of slow convergence. While Newton methods will converge in far fewer iterations, the time required per inversion iteration can be prohibitively expensive. A more promising approach would be the use of an approximate preconditioner that when applied to the conjugate gradient search direction becomes an approximation to the Newton direction. We refer the interest reader to Newman and Boggs (2004), where the technique is demonstrated for 3D EM inverse problem for frequency domain data.

Another approach in accelerating convergence is to consider Quasi-Newton methods. These methods use error functional gradients at the current and prior inversion iterations to construct an approximate Hessian or its corresponding inverse. As the

iteration procedure continues, the approximation continues to improve in principle, converging to the true Hessian or its inverse at the functional minimum. These methods can be seen as extensions of the conjugate gradient method, in which additional storage is used to accelerate convergence; they also require a line search procedure. Unfortunately in large-scale inverse problems, the Quasi-Newton methods are not that practical due to excessive storage requirements. This problem can be avoided by implementing a limited memory variant of the scheme (cf. Liu and Nocedal, 1989). In a limited memory Quasi-Newton scheme, the Hessian or its inverse are never formed explicitly as this would require too much storage, but rather $i+1$ previous values for functional gradients and model updates (i is specified by the user) are stored as vectors, and efficiently used to construct matrix-vector products involving the Hessian, needed to obtain the next model update. These methods can also be further accelerated using preconditioning techniques previously described.

ACKNOWLEDGEMENTS

This work would not have been possible without the invitation and support of Professor Fritz Neubauer to host G. A. Newman as a guest scholar at the Institute of Geophysics and Meteorology, University of Cologne from 2000 to 2001. We dedicate this paper to Fritz Neubauer in honor of his career and upon his recent retirement. We also acknowledge Martyn Unsworth, Michael Zdhanov, Max Meju and Eldad Haber for suggestions that improved the readability and quality of the paper. This work was carried out at the University of Cologne, Sandia National Laboratories and Lawrence Berkeley National Laboratory with United States Department of Energy, Office of Basic Energy

Sciences funding. Additional support for G. A. Newman was provided by a Mercator Fellowship, granted by the Deutsche Forschungsgemeinschaft (DFG); Michael Commer also received financial support from the German Academic Exchange Service (DAAD). Sandia is a multi-program laboratory operated by the Sandia Corporation, a Lockhead Martin Company, for the United States Department of Energy under Contract DE-AC04-94AL85000.

REFERENCES

Chan J., Haber E., and Oldenburg D., 2002, Three-dimensional numerical modeling and inversion of magnetometric resistivity data: Geophys. J. Int., **149**, 679-697.

Chew W. C., 1990, Waves and Fields in Inhomogeneous Media, Van Nostrand Reinhold.

Claerbout J. F., 1971, Toward a unified theory of reflector mapping, Geophysics, **36**, 467-481.

Commer M. and Newman G. A., 2004, A parallel finite-difference approach for three-dimensional transient electromagnetic modeling with non-causal sources: Geophysics, In Press.

Commer M., 2004, Three-dimensional inversion of transient electromagnetic data: A comparative study: PhD Thesis, University of Cologne.

Druskin, V., and Knizhnerman, L., 1994, Spectral approach to solving three-dimensional Maxwell's equations in the time and frequency domains: Radio Science, **29**, 937-953

Eaton P. A., and Hohmann G. W., 1989, A rapid inversion technique for transient electromagnetic soundings, Phys. Earth Planet Inter., **53**, 394-404.

Felsen L. B., and Marcuritz N., 1973, Radiation and Scattering of Waves, Prentice-Hall.

Fullagar P. K., 1989, Generation of conductivity-depth pseudo-sections from coincident loop and in-loop TEM data, Explor. Geophys. **20**, 43-45.

Gropp, W., Lusk E., and Skjellum A., 1999, Using MPI: Portable Parallel Programming with the Message-Passing Interface, MIT Press.

Gunderson B. M., Newman G. A., and Hohmann, G. W., 1986, Three-dimensional transient electromagnetic responses for a grounded source, Geophysics, **51**, 2117-2130.

Haber E. and Oldenburg, D., 1997, Joint inversion a structural approach: Inverse Problems, **13**, 63-77.

Haber E., and Oldenburg D., 2002, Inversion of 3D time domain electromagnetic data using an all-at-once approach: Expanded Abstracts, Soc. Expl. Geophys. 72nd Annual Meeting, Salt Lake City, Utah.

Hohmann G. W., and Ward, S. H., 1988, Electromagnetic theory for geophysical applications: Soc. Expl. Geophys.

Hördt A. and Mueller M., 2000, Understanding LOTEM data from mountainous terrain, Geophysics, **65**, 1-11.

Hördt, A., Dautel, S., Tezkan, B., and Thern, H., 2000, Interpretation of long-offset transient electromagnetic data from the Odenwald area, Germany, using two-dimensional modelling, Geophys. J. Int., **140**, 577-586.

Hördt, A., 1998, Calculation of electromagnetic sensitivities in the time domain, Geophys. J. Int., **133**, 713 720.

Hördt, A., Druskin, V. L., Knizhnerman, L. A., and Strack, K. M., 1992, Interpretation of 3-D effects in long-offset transient electromagnetic (LOTEM) soundings in the Muensterland area, Germany, Geophysics, **57,** 1127-1137.

Liu D. C. and Nocedal, J., 1989, On limited memory BFGS Method for large scale optimization: Mathematical Programming, **45** 503-528.

Macnae, J. C., and Lamontagne, Y., 1987, Imaging quasilayered conductivity structures by simple processing of transient electromagnetic data, Geophysics, **52**, 545 554.

Macnae, J. C., Smith, R., Polzer B. D., Lamontagne Y., 1991, Conductivity-depth imaging of airborne electromagnetic step-response data, Geophysics, **56**, 102 114.

Nabighian, M. N., and Macnae, J. C., 1991, Time domain electromagnetic prospecting methods, *in* Electromagnetic Methods in Applied Geophysics Vol. 2, Application, Part A, M.N. Nabighian Ed., Soc. Expl. Geophys.

Newman, G. A., Anderson, W. L., and Hohmann, G. W., 1987, Interpretation of three dimensional transient electromagnetic soundings for the central loop configuration: Geophys. J. R. astr. Soc., **89**, 889-914.

Newman G. A., and Alumbaugh, D. L., 1997, Three-dimensional massively parallel electromagnetic inversion – I. Theory: Grophys. J. Int., **128**, 345-354.

Newman, G. A., and Alumbaugh, D. L., 2000, Three-dimensional magnetotelluric inversion using non-linear conjugate gradients, Geophys. J. Int., **140**, 410-424.

Newman, G. A. and Boggs, P., 2004, Solution accelerators for large scale 3D electromagnetic inverse problems: submitted to Inverse Problems.

Nekut, A. G., 1987, Direct inversion of time-domain electromagnetic data, Geophysics, **52**, 1431-1435.

Pellerin L., and Alumbaugh, D. L., 1997, Tools for electromagnetic investigation of the shallow subsurface, The Leading Edge, **16**, No. 11, Soc. Expl. Geophys.

Tai C., 1990, *Generalized vector and dyadic analysis*, IEEE Press.

Tarantola A., 1984, Inversion of seismic reflection data in the acoustic approximation, Geophysics, **49**, 1259-1266.

Tikhonov A. N., and Arsennin, V. Y., 1977, Solutions to Ill Posed Problems, John Wiley.

Tuminaro R., S., Heroux, M., Hutchinson, S. A., and Shadid, J. N., 1999, Official AZTEC Users Guide Version 2.1, Sandia National Laboratories Sand Report SAND99-8801J.

Wang T., Oristaglio, M., Tripp A., and Hohmann, G. W., 1994, Inversion of diffusive transient electromagnetic data by a conjugate gradient method, Radio Science, **29**, 1143-1156.

Wang, T. and Hohmann, G. W., 1993, A finite-difference, time-domain solution for three-dimensional electromagnetic modeling, Geophysics, **58**, 797-809.

Zhdanov, M. S., 2002, *Geophysical inverse theory and regularization problems*, Elsevier.

Zhdanov M. S., Pavlov, D. A., Ellis, R. G., 2002, Localized S-inversion of time-domain electromagnetic data, Geophysics, **67**, 1115-1125.

Zhdanov M. S. and Pavlov, D. A., 2001, Analysis and interpretation of anomalous conductivity and magnetic permeability effects in time domain electromagnetic data Part II: $S\mu$-inversion: J. App. Geophys., **46**, 235-248.

Zhdanov M. S. and Portniaguine, O., 1997, Time-domain electromagnetic migration in the solution of inverse problems: Geophys. J. Int., **131**, 293-309.

Zhdanov M. S. and Frenkel M. A., 1983, The solution of inverse problems on the basis of the analytic continuation of the transient electromagnetic field in reverse time, J. Geomagn. Geoelectr., **35**, 747-765.

FIGURE CAPTIONS

Figure 1. Illustrated are surface and borehole TEM measurement configurations, typically deployed in geophysical field investigations.

Figure 2. Checks on the gradients are shown for vertical magnetic dipole sourcing. Panel a) shows gradient comparisons for electric field data (y-component) plotted as a percentage difference, $100*\| \gamma_\sigma^{e_y}(r') - {}^{p}\gamma_\sigma^{e_y}(r') \| / \| \gamma_\sigma^{e_y}(r') \|$. Panel b) shows the

corresponding comparisons for voltage data (z component), $100*\| \gamma_{\sigma}^{u_z}(r') - {}^{p}\gamma_{\sigma}^{u_z}(r') \| / \| \gamma_{\sigma}^{u_z}(r') \|$, and panel c) for magnetic field data (z component), $100*\| \gamma_{\sigma}^{h_z}(r') - {}^{p}\gamma_{\sigma}^{h_z}(r') \| / \| \gamma_{\sigma}^{h_z}(r') \|$.

Figure 3. Checks are shown on the gradients for horizontal (y-directed) electric dipole sourcing. Panel a) shows gradient comparisons for electric field data (y component) plotted as a percentage difference, $100*\| \gamma_{\sigma}^{e_y}(r') - {}^{p}\gamma_{\sigma}^{e_y}(r') \| / \| \gamma_{\sigma}^{e_y}(r') \|$. Panel b) shows the corresponding comparisons for voltage data (z component), where the percentage difference is given by the expression $100*\| \gamma_{\sigma}^{u_z}(r') - {}^{p}\gamma_{\sigma}^{u_z}(r') \| / \| \gamma_{\sigma}^{u_z}(r') \|$.

Figure 4. Comparison of gradients for vertical magnetic field data computed using back propagation and perturbation, arising from vertical magnetic dipole sourcing. Comparison is plotted as a percentage difference, $100*\| \gamma_{\sigma}^{h_z}(r') - {}^{p}\gamma_{\sigma}^{h_z}(r') \| / \| \gamma_{\sigma}^{h_z}(r') \|$ and uses a finer computational mesh. In the x-direction outside the receiver well, the mesh now consists of nodes placed at 100, 105, 110, 115, 120, 130, 140, 150, 170 and 200 meters instead of nodes places at 100, 110, 130, 160, and 200 meters, as before. Significant improvement is observed for images points near the receiver well (compare with panel c) in Figure 2).

Figure 5. Simple three-dimensional model used to test the imaging scheme for LOTEM field sourcing.

Figure 6. Shown are the LOTEM transmitter and receiver geometry used to reconstruct the model in Figure 5. Also shown is the reconstructed conductivity model at the surface of the Earth.

Figure 7. The normalized error functional (equation (5)) is plotted against inversion iteration (dashed curve) for electric field and voltage data. The solid curve corresponds to the data error component of the normalized error functional.

Figure 8. Data fits for electric field for center profile (Y = 0 m) over the target body in Figure 6 for six different delay times, ranging from 1 to 50 ms; dotted curves are the observations and solid curves the predicted data. The figure also shows the corresponding data fit after the first inversion iteration (dashed), demonstrating the significant improvement in the data fit as the model is iterated.

Figure 9. Data fits for voltage for center profile (Y = 0 m) over the target body in Figure 6 for six different delay times, ranging from 1 to 50 ms; dotted curves are the observations and solid curves the predicted data. The figure also shows the corresponding data fit after the first inversion iteration (dashed).

Figure 10. Two cross sections of the reconstructed model are shown. The x-z cross section (y=0 m) bisects the transmitter in Figure 5 and 6, while the y-z cross section is located at x=300 m. The actual location of the target body is indicated by the white rectangles.

Figure11. The reconstructed model at 100 m depth. The actual location of the target body is indicated by the white square.

Figure 12. Two cross sections of the reconstructed model for first inversion iteration are shown. These imaging results also correspond to the migration of the initial data errors into the model. The x-z cross section (y=0 m) bisects the transmitter in Figure 5 and 6, while the y-z cross section is located at x=300 m. The actual location of the target body is indicated by the white rectangles.

Figure 13. The reconstructed model for the first inversion iteration at 100 m depth is illustrated, where the actual location of the target body is indicated by the white square. This imaging result also corresponds to the migration of the initial data errors into the model.

Figure 14. Complex three-dimensional model used to test the imaging scheme for the long offset transient electromagnetic (LOTEM) field sourcing.

Figure 15. Shown are the LOTEM receiver geometry used to reconstruct the model shown in Figure 14. Also shown is the reconstructed conductivity model at the surface of the Earth.

Figure 16. The normalized error functional (equation (5)) is plotted against inversion iteration (dashed curve) for electric field and voltage data. The solid curve corresponds to the data error component of the normalized error functional.

Figure 17. Data fits for electric field for selected profiles Y = 81m (black) , -12m (red) and –81 m (blue) , shown in Figure 15, for eight different delay times ranging from 0.1 to 10 ms. Solid curves depict the predicted data (65^{th} inversion iteration) and dotted curves the observations.

Figure 18. Data fits for voltage for selected profiles Y = 81m (black) , -12m (red) and –81 m (blue) , shown in Figure 15, for eight different delay times ranging from 0.1 to 5 ms. Solid curves depict the predicted data (65^{th} inversion iteration) and dotted curves the observations.

Figure19. The reconstructed model at 20 m depth is illustrated, where the actual location of the near surface bodies are indicated by the white rectangles.

Figure 20. Three x-z cross sections of the reconstructed model are shown. The top, middle and bottom cross sections are located respectively at Y=62.5 m, 0 m and 100 m. Note further that the middle cross section (Y=0 m) also bisects the transmitter in Figure 14. The locations and geometries of the 3D targets bodies are indicated by the white rectangles.

APPENDIX A

DYADIC GREEN FUNCTIONS FOR ELECTROMAGNETIC INDUCTION

In the quasi-static limit, solutions of Maxwell's equations (3) and (4) can be expressed using dyadic Green functions for non-causal sourcing as

$$\mathbf{e}(\mathbf{r},t)=\int_{v'}\int_{-\infty}^{t}\mathbf{G}_{11}(\mathbf{r},t\,|\,\mathbf{r}',t')\cdot\mathbf{j}(\mathbf{r}',t')\,dt'\,d\mathbf{r}'+\int_{v'}\int_{-\infty}^{t}\frac{\mathbf{G}_{12}(\mathbf{r},t\,|\,\mathbf{r}',t')}{\mu(\mathbf{r}')}\cdot\mathbf{m}(\mathbf{r}',t')\,dt'\,d\mathbf{r}' \quad \text{(A1)}$$

and

$$\mathbf{h}(\mathbf{r},t)=\int_{v'}\int_{-\infty}^{t}\mathbf{G}_{21}(\mathbf{r},t\,|\,\mathbf{r}',t')\cdot\mathbf{j}(\mathbf{r}',t')\,dt'\,d\mathbf{r}'+\int_{v'}\int_{-\infty}^{t}\frac{\mathbf{G}_{22}(\mathbf{r},t\,|\,\mathbf{r}',t')}{\mu(\mathbf{r}')}\cdot\mathbf{m}(\mathbf{r}',t')\,dt'\,d\mathbf{r}' \quad \text{(A2)}$$

where (v,t) is the space-time domain over which the sources act. Here $\mathbf{j}$ denotes the electric source current and $\mathbf{m}$ the magnetic source current, which is equivalent to

$$\mathbf{m}(\mathbf{r},t)=\mu(\mathbf{r})\,\partial\mathbf{m}_{\mathbf{p}}(\mathbf{r},t)/\partial t\,. \quad \text{(A3)}$$

The magnetization vector, $\mathbf{m}_{\mathbf{p}}(\mathbf{r},t)$, can be regarded as an integrated surface current (Hohmann and Ward, 1988).

The meaning of each Green dyadic is interpreted, for example, as follows: if $\hat{\mathbf{x}}$ and $\hat{\mathbf{z}}$ are unit vectors in the x and z directions, then $\hat{\mathbf{x}}\cdot\mathbf{G}_{21}(\mathbf{r},t\,|\,\mathbf{r}',t')\cdot\hat{\mathbf{z}}$ is the x component of the magnetic field at point $\mathbf{r}$ and time t caused by an impulsive electric current (an electric dipole) oriented in the z direction at point $\mathbf{r}'$ and t'. In analogous fashion $\hat{\mathbf{x}}\cdot\mathbf{G}_{12}(\mathbf{r},t\,|\,\mathbf{r}',t')\cdot\hat{\mathbf{z}}$ is the x component of the electric field at point $\mathbf{r}$ and time t caused by an impulsive magnetic current (a magnetic dipole) oriented in the z direction at point $\mathbf{r}'$ and t'.

The four dyadics satisfy the following first-order equations (ζ is the identity dyadic),

$$\sigma \mathbf{G}_1 - \nabla \mathrm{x} \mathbf{G}_2 = -\zeta(\mathbf{r}-\mathbf{r}')\delta(t-t'), \tag{A4}$$

$$\nabla \mathrm{x} \mathbf{G}_1 + \mu \partial \mathbf{G}_2 / \partial t = 0, \tag{A5}$$

$$\sigma \mathbf{G}_2 - \nabla \mathrm{x} \mathbf{G}_2 = 0, \tag{A6}$$

$$\nabla \mathrm{x} \mathbf{G}_2 + \mu \partial \mathbf{G}_2 / \partial t = -\zeta(\mathbf{r}-\mathbf{r}')\mu(\mathbf{r})\delta(t-t') \tag{A7}$$

and are causal,

$$\mathbf{G}_{ij}(\mathbf{r}, t \mid \mathbf{r}', t') \equiv \mathbf{0}, \quad t \le t'. \tag{A8}$$

Equations (A6) and (A7) give the electromagnetic fields arising for magnetic dipole sourcing, where the time dependence of the magnetization for the dipole is based upon a Heavyside step function: $\mathrm{u(t)}=\begin{Bmatrix} 1; t \ge 0 \\ 0; t < 0 \end{Bmatrix}$ and when time differentiated in equation (A3) this produces the delta function response in time in equation (A7). Also needed are the adjoint Green dyadics $\mathbf{G}_{ij}^{+}$,which are obtained from (A4)-(A7) by reversing the sign of all space-time coordinates (Felsen and Marcuvitz, 1973),

$$\sigma \mathbf{G}_{11}^{+} + \nabla \mathrm{x} \mathbf{G}_{21}^{+} = -\zeta(\mathbf{r}-\mathbf{r}')\delta(t-t'), \tag{A9}$$

$$-\nabla \mathrm{x} \mathbf{G}_{11}^{+} - \mu \partial \mathbf{G}_{21}^{+} / \partial t = 0, \tag{A10}$$

$$\sigma \mathbf{G}_{12}^{+} + \nabla \mathrm{x} \mathbf{G}_{22}^{+} = 0, \tag{A11}$$

$$-\nabla \mathrm{x} \mathbf{G}_{12}^{+} - \mu \partial \mathbf{G}_{22}^{+} / \partial t = -\zeta(\mathbf{r}-\mathbf{r}')\mu(\mathbf{r})\delta(t-t') \tag{A12}$$

and are anticausal,

$$\mathbf{G}_{ij}^{+}(\mathbf{r}, t \mid \mathbf{r}', t') \equiv \mathbf{0}, \quad t \ge t'. \tag{A13}$$

Reciprocal Relationships of the Dyadic Green Functions

At this point, it needs to be emphasized that both $\mathbf{G}_{ij}$ and $\mathbf{G}_{ij}^{+}$ always propagate the impulse response of a field. Care must be taken when specifying the reciprocal

relationships between the various Dyadic Green Functions and the corresponding adjoint forms when $i \neq j$, which involves the reciprocity relationship between the electric field impulse response of a magnetic dipole and vice versa, the magnetic field impulse response of an electric dipole. It can be shown (see Hördt, 1998) that the magnetic field impulse response for the electric dipole is equivalent to the electric field step response for a magnetic dipole. This is a critical point not taken into account in the Wang et al. (1994) gradient specifications, leading to incorrect results for gradients involving magnetic field data types. As an example, the magnetic field gradient for conductivity will ultimately involve a back-propagated electric field step response, while in Wang et al. (1994), it is incorrectly specified using a back-propagated electric field. It turns out however, that the two types of back-propagated fields are related to each other through a simple time differentiation. The authors did not recognize the problem, because they presented synthetic conductivity inversion examples for electric field data, where the gradients for this data type were correctly specified.

The correct reciprocal relationships between the Green dyadics and their corresponding adjoints are as follows:

$$\mathbf{G}_{11}^{+}(\mathbf{r}',t'|\mathbf{r},t) = \tilde{\mathbf{G}}_{11}(\mathbf{r},t|\mathbf{r}',t') \tag{A14}$$

$$\mathbf{G}_{12}^{+}(\mathbf{r}',t'|\mathbf{r},t) = -\mu(\mathbf{r})\frac{\partial \tilde{\mathbf{G}}_{21}(\mathbf{r},t|\mathbf{r}',t')}{\partial t} \tag{A15}$$

$$\mu(\mathbf{r}')\frac{\partial \mathbf{G}_{21}^{+}(\mathbf{r}',t'|\mathbf{r},t)}{\partial t'} = \tilde{\mathbf{G}}_{12}(\mathbf{r},t|\mathbf{r}',t') \tag{A16}$$

$$\mu(\mathbf{r}')\mathbf{G}_{22}^{+}(\mathbf{r}',t'|\mathbf{r},t) = \mu(\mathbf{r})\tilde{\mathbf{G}}_{22}(\mathbf{r},t|\mathbf{r}',t')\,. \tag{A17}$$

Here, the tilde (~) indicates the transpose of a dyadic (e.g., $\hat{\mathbf{x}}\cdot\mathbf{G}_{11}\cdot\hat{\mathbf{z}} = \hat{\mathbf{z}}\cdot\tilde{\mathbf{G}}_{11}\cdot\hat{\mathbf{x}}$). In order to make equations (A15 and A16) dimensionally consistent, it is understood that units of seconds (sec) or its inverse ($\sec^{-1}$) must be introduced to the left hand side of these equations, because equivalent quantities do not necessarily have the same units or dimensions. We note that Felsen and Marucvitz (1973, pages 9 to 14) have shown how to rigorously derive reciprocity relations for the tensor Green's functions in vacuum. Equations (A14) through (A17) represent an extension of their derivation for treatment of lossy media in the quasi-static limit (no displacement currents) that incorporates the correct description of the magnetic source current given by equation (A3). It is important to note that equation (A16) is similar to (A15), except for the sign change, which is required because the field evolves in reverse time, starting at time *t*.

When equation (A15) is integrated over time t and (A16) over time t', it follows

$$ {}^{step}\mathbf{G}^{+}_{12}(\mathbf{r}',t'|\,\mathbf{r},t) = \mu(\mathbf{r})\tilde{\mathbf{G}}_{21}(\mathbf{r},t\,|\,\mathbf{r}',t') \tag{A18}$$

$$ -\mu(\mathbf{r})\mathbf{G}^{+}_{21}(\mathbf{r}',t'|\,\mathbf{r},t) = {}^{step}\tilde{\mathbf{G}}_{12}(\mathbf{r},t\,|\,\mathbf{r}',t') \tag{A19}$$

where,

$$ {}^{step}\mathbf{G}^{+}_{12}(\mathbf{r}',t'|\,\mathbf{r},t) = \int_{t}^{t'} dt\,\mathbf{G}^{+}_{12}(\mathbf{r}',t'|\,\mathbf{r},t) \tag{A20}$$

$$ {}^{step}\tilde{\mathbf{G}}_{12}(\mathbf{r},t\,|\,\mathbf{r}',t') = \int_{t'}^{t} dt'\tilde{\mathbf{G}}_{12}(\mathbf{r},t\,|\,\mathbf{r}',t') \quad . \tag{A21}$$

APPENDIX B

GRADIENT SPECIFICATION FOR ELECTRIC FIELD DATA

To make the derivation that follows more manageable we first consider the problem for a single source excitation and drop the dependence on source excitation, $\mathbf{s}_j$. When the derivation is complete for this problem it is easy to extend the gradient for multiple source locations using superposition of the gradients for different source excitations. We will proceed similarly for gradient derivations involving voltage and magnetic field data in Appendices C and D.

For small model perturbations, one can use equation (1) for electric field data to show that

$$\delta\vartheta(\sigma,\mu) = -\sum_i \int_0^T \frac{dt}{t}\ \delta\mathbf{e}^{\circ}(\mathbf{r}_i,t)\cdot\delta\mathbf{e}(\mathbf{r}_i,t)\ , \tag{B1}$$

where $\delta\mathbf{e}$ is the change in the calculated electric field data when the conductivity and permeability are changed. Now for small perturbations $\delta\sigma(\mathbf{r}')$ and $\delta\mu(\mathbf{r}')$ about the current model, the change in the error functional, can also be written as

$$\delta\vartheta(\sigma,\mu) = \vartheta(\sigma+\delta\sigma,\mu+\delta\mu) - \vartheta(\sigma,\mu) \approx < \gamma_\sigma, \delta\sigma > + < \gamma_\mu, \delta\mu >, \tag{B2}$$

since the gradients are Fréchet derivatives of the error functional $\gamma_\sigma = \delta\vartheta(\sigma,\mu)/\delta\sigma$ and $\gamma_\mu = \delta\vartheta(\sigma,\mu)/\delta\mu$. In equation (B2) the inner product is defined as

$$< \gamma, \delta m > = \int_{v'} \gamma(\mathbf{r}')\delta m(\mathbf{r}')\, d\mathbf{r}', \tag{B3}$$

where δm stands for either $\delta\sigma$ or $\delta\mu$ and *v'* is the domain which the model is allowed to vary.

If we perturb the fields and model in Maxwell's equations (equations (3) and (4)), where

$\sigma \rightarrow \sigma + \delta\sigma$

$\mu \rightarrow \mu + \delta\mu$

$\mathbf{h} \rightarrow \mathbf{h} + \delta\mathbf{h}$

$\mathbf{e} \rightarrow \mathbf{e} + \delta\mathbf{e}$

and subtract the Maxwell's equations for the non-perturbed state, then dropping terms involving the product of two perturbed quantities gives

$$\sigma\delta\mathbf{e} - \nabla \mathrm{X} \delta\mathbf{h} = -\delta\sigma\,\mathbf{e} \tag{B4}$$

and

$$\nabla \mathrm{X} \delta\mathbf{e} + \mu\,\partial\delta\mathbf{h} / \partial t = -\delta\mu \frac{\partial}{\partial t}\mathbf{h}. \tag{B5}$$

The solution to the perturbed electric field is given as

$$\begin{aligned} \delta\mathbf{e}(\mathbf{r},t) &= \int_{v'} \int_{-\infty}^{t} \mathbf{G}_{11}(\mathbf{r},t \mid \mathbf{r}',t') \cdot \mathbf{e}(\mathbf{r}',t')\, \delta\sigma(\mathbf{r}')\, dt'\, d\mathbf{r}' \\ &+ \int_{v'} \int_{-\infty}^{t} \frac{\mathbf{G}_{12}(\mathbf{r},t \mid \mathbf{r}',t')}{\mu(\mathbf{r}')} \cdot \frac{\partial}{\partial t'}\mathbf{h}(\mathbf{r}',t')\delta\mu(\mathbf{r}')\, dt'\, d\mathbf{r}'. \end{aligned} \tag{B6}$$

Substituting equation (B6) into equation (B1) and noting equations (B2) and (B3) yields

$$\gamma_{\sigma}^{e}(\mathbf{r}') = -\sum_{i} \int_{0}^{T} \frac{dt}{t}\, \delta\mathbf{e}^{o}(\mathbf{r}_i,t) \int_{-\infty}^{t} dt'\, \mathbf{G}_{11}(\mathbf{r}_i,t \mid \mathbf{r}',t')\, \mathbf{e}(\mathbf{r}',t') \tag{B7}$$

and

$$\gamma_{\mu}^{e}(\mathbf{r}') = -\sum_{i} \int_{0}^{T} \frac{dt}{t}\, \delta\mathbf{e}^{o}(\mathbf{r}_i,t) \int_{0}^{t} dt' \frac{\mathbf{G}_{12}(\mathbf{r}_i,t \mid \mathbf{r}',t')}{\mu(\mathbf{r}')} \frac{\partial}{\partial t'}\mathbf{h}(\mathbf{r}',t'). \tag{B8}$$

The gradients $\gamma_\sigma^e(\mathbf{r}')$ and $\gamma_\mu^e(\mathbf{r}')$ at a model point $\mathbf{r}'$ correspond to partial derivatives of the error functional $\vartheta(\sigma,\mu)$ with respect to the conductivity and permeability at that point. Thus, for example, equation (B7) indicates that the partial derivative of $\vartheta(\sigma,\mu)$ with respect to the conductivity at $\mathbf{r}'$ is obtained by correlating the electric-field errors $\delta\mathbf{e}^o$ at all measurement points with the electric field caused by a point electric dipole current source at $\mathbf{r}'$ that has the same direction and the same time dependence as the electric field at $\mathbf{r}'$ in the current model.

Wang et al. (1994) remark that equations (B7) and (B8) require one forward simulation to compute the fields in the current model and many more forward simulations as there are image points to compute the gradients and this quickly becomes impractical as the number of image points becomes large. They also showed how to put these equations into an efficient form for computation of the gradients by reversing the order of the time integrations and using adjoint dyadics, where

$$
\begin{aligned}
\gamma_\sigma^e(\mathbf{r}') &= -\sum_i \int_0^T dt\ \frac{\delta\mathbf{e}^o(\mathbf{r}_i,t)}{t} \int_{-\infty}^{t} dt'\mathbf{G}_{11}(\mathbf{r}_i,t\,|\,\mathbf{r}',t')\,\mathbf{e}(\mathbf{r}',t') \\
&= -\sum_i \int_{-\infty}^{T} dt' \int_{t'}^{T} \frac{\delta\mathbf{e}^o(\mathbf{r}_i,t)}{t}\mathbf{G}_{11}(\mathbf{r}_i,t\,|\,\mathbf{r}',t')\,\mathbf{e}(\mathbf{r}',t')\,dt \\
&= -\sum_i \int_{-\infty}^{T} dt' \int_{t'}^{T} \mathbf{e}(\mathbf{r}',t')\,\mathbf{G}_{11}^{+}(\mathbf{r}',t'|\,\mathbf{r}_i,t)\,\frac{\delta\mathbf{e}^o(\mathbf{r}_i,t)}{t}\,dt \\
&= \int_{-\infty}^{T} dt'\ \mathbf{e}(\mathbf{r}',t')\cdot\sum_i \int_{T}^{t'} dt\ \mathbf{G}_{11}^{+}(\mathbf{r}',t'|\,\mathbf{r}_i,t)\,\frac{\delta\mathbf{e}^o(\mathbf{r}_i,t)}{t} \\
&= \int_{-\infty}^{T} dt'\ \mathbf{e}(\mathbf{r}',t')\cdot\mathbf{e}_b(\mathbf{r}',t'|\,\delta\mathbf{e}^o)\,. \qquad \text{(B9)}
\end{aligned}
$$

Equation (B9) uses the reciprocity relationship in equation (A14) in the form of

$$\mathbf{e}(\mathbf{r}',t')\cdot\mathbf{G}_{11}^{+}(\mathbf{r}',t'|\mathbf{r}_i,t)\cdot\frac{\delta\mathbf{e}^o(\mathbf{r}_i,t)}{t}=\frac{\delta\mathbf{e}^o(\mathbf{r}_i,t)}{t}\cdot\mathbf{G}_{11}(\mathbf{r}_i,t|\mathbf{r}',t')\cdot\mathbf{e}(\mathbf{r}',t') \tag{B10}$$

and defines a back-propagated field, where

$$\mathbf{e}_b(\mathbf{r}',t'|\,\delta\mathbf{e}^o)=\sum_i\int_T^{t'}dt\,\mathbf{G}_{11}^{+}(\mathbf{r}',t'|\,\mathbf{r}_i,t)\,\frac{\delta\mathbf{e}^o(\mathbf{r}_i,t)}{t}\,. \tag{B11}$$

Since $t'< t$ in the above integral it has the correct form for propagation with the adjoint Green dyadic $\mathbf{G}_{11}^{+}(\mathbf{r}',t'|\,\mathbf{r}_i,t)$. This dyadic gives the electric field at $\mathbf{r}'$ and t' caused by an electric current source (here $\delta\mathbf{e}^o$) radiating at $\mathbf{r}_i$ at a later time *t*. The reversal of the time order is implicit in the definition of the adjoint Green dyadics, because they are anti-causal.

Using a similar series of steps for the magnetic permeability gradient $\gamma_u(\mathbf{r}')$ we have

$$\begin{aligned}\gamma_\mu^e(\mathbf{r}')&=-\sum_i\int_0^T dt\;\frac{\delta\mathbf{e}^o(\mathbf{r}_i,t)}{t}\int_0^t dt'\frac{\mathbf{G}_{12}(\mathbf{r}_i,t\,|\,\mathbf{r}',t')}{\mu(\mathbf{r}')}\,\frac{\partial}{\partial t'}\mathbf{h}(\mathbf{r}',t')\\&=-\sum_i\int_0^T dt'\int_{t'}^T\frac{\delta\mathbf{e}^o(\mathbf{r}_i,t)}{t}\,\frac{\mathbf{G}_{12}(\mathbf{r}_i,t\,|\,\mathbf{r}',t')}{\mu(\mathbf{r}')}\,\frac{\partial}{\partial t'}\mathbf{h}(\mathbf{r}',t')\,dt\\&=\int_0^T dt'\,\frac{\partial}{\partial t'}\mathbf{h}(\mathbf{r}',t')\cdot\sum_i\int_T^{t'}dt\,\frac{\partial}{\partial t'}\mathbf{G}_{21}^{+}(\mathbf{r}',t'|\,\mathbf{r}_i,t)\,\frac{\delta\mathbf{e}^o(\mathbf{r}_i,t)}{t}\\&=\int_0^T dt'\,\frac{\partial}{\partial t'}\mathbf{h}(\mathbf{r}',t')\cdot\frac{\partial}{\partial t'}\mathbf{h}_b(\mathbf{r}',t'|\,\delta\mathbf{e}^o)\;.\end{aligned} \tag{B12}$$

In deriving equation (B12) we also defined a back-propagated magnetic field

$$\mathbf{h}_b(\mathbf{r}',t'|\,\delta\mathbf{e}^o)=\sum_i\int_T^{t'}dt\;\mathbf{G}_{21}^{+}(\mathbf{r}',t'|\,\mathbf{r}_i,t)\,\frac{\delta\mathbf{e}^o(\mathbf{r}_i,t)}{t} \tag{B13}$$

and employed the reciprocity relationship based upon equation (A16),

$$\frac{\partial}{\partial t'}\mathbf{h}(\mathbf{r}',t')\cdot\frac{\partial}{\partial t'}\mathbf{G}_{21}^{+}(\mathbf{r}',t'|\,\mathbf{r}_i,t)\cdot\frac{\delta\mathbf{e}^o(\mathbf{r}_i,t)}{t}=\frac{\delta\mathbf{e}^o(\mathbf{r}_i,t)}{t}\cdot\frac{\mathbf{G}_{12}(\mathbf{r}_i,t\,|\mathbf{r}',t')}{\mu(\mathbf{r}')}\cdot\frac{\partial}{\partial t'}\mathbf{h}(\mathbf{r}',t')\,. \tag{B14}$$

Because the back-propagated fields in equations (B11) and (B13) are based upon the adjoint dyadics $\mathbf{G}_{11}^{+}(\mathbf{r}',t'|\mathbf{r}_i,t)$ and $\mathbf{G}_{21}^{+}(\mathbf{r}',t'|\mathbf{r}_i,t)$, this implies that the back-propagated fields $\mathbf{e}_b$ and $\mathbf{h}_b$ satisfy the adjoint Maxwell equations that are sourced using the data differences $\delta\mathbf{e}^o$ at all the receiver positions radiating as electrical current sources in reverse time; that is

$$\sigma\mathbf{e}_b + \nabla \mathrm{x}\mathbf{h}_b = -\sum_i \frac{\delta\mathbf{e}^o(\mathbf{r}_i,t)}{t}\delta(\mathbf{r}-\mathbf{r}_i) \tag{B15}$$

$$\nabla \mathrm{x}\mathbf{e}_b + \mu\,\partial\mathbf{h}_b/\partial t = 0 \tag{B16}$$

from time $t = T$ to $-\infty$. These equations follow directly from equations (A9) and (A10), (B11) and (B13).

A significant disadvantage of equation (B9) is the requirement that the back-propagated fields in equations (B15) and (B16) be computed before time 0. Here, it is computationally convenient to reformulate the gradient in equation (B9), such that

$$\gamma_\sigma^e(\mathbf{r}') = \int_0^T dt'\,\{\mathbf{e}(\mathbf{r}',t') - \mathbf{e}_{DC}(\mathbf{r}')\}\cdot\mathbf{e}_b(\mathbf{r}',t'|\,\delta\mathbf{e}^o) + \mathbf{e}_{DC}(\mathbf{r}')\cdot\int_{-\infty}^T dt'\,\mathbf{e}_b(\mathbf{r}',t'|\,\delta\mathbf{e}^o) \tag{B17}$$

where the DC electric field $\mathbf{e}_{DC}(\mathbf{r}') = \mathbf{e}(\mathbf{r}',t')$ when $t' \le 0$, is determined by solving the Maxwell equations (equations (3) and (4)) in the steady state limit. Now the last term in equation (B17) suggests that we integrate the equations (B15) and (B16),

$$\sigma\int_{-\infty}^T dt\,\mathbf{e}_b + \nabla \mathrm{x}\int_{-\infty}^T dt\,\mathbf{h}_b = -\sum_i \int_0^T dt\;\frac{\delta\mathbf{e}^o(\mathbf{r}_i,t)}{t}\,\delta(\mathbf{r}-\mathbf{r}_i) \tag{B18}$$

and

$$-\nabla \mathrm{x}\int_{-\infty}^{T} dt\,\mathbf{e}_b - \mu_o \int_{-\infty}^{T} dt\;\partial \mathbf{h}_b / \partial t = 0. \tag{B19}$$

We have truncated the integration in the source term to $-\sum_i \int_0^T dt\;\frac{\delta \mathbf{e}^o(\mathbf{r}_i,t)}{t}\,\delta(\mathbf{r}-\mathbf{r}_i)$, because $\delta\mathbf{e}^o(\mathbf{r}_i,t) = 0$ for $t<0$. Thus the integrated back-propagated fields simplify to

$$\sigma \mathbf{e}_b^{DC} + \nabla \mathrm{x}\mathbf{h}_b^{DC} = -\sum_i \int_0^T dt\,\frac{\delta \mathbf{e}^o(\mathbf{r}_i,t)}{t}\,\delta(\mathbf{r}-\mathbf{r}_i) \tag{B20}$$

$$\nabla \mathrm{x}\mathbf{e}_b^{DC} = 0, \tag{B21}$$

because $\mathbf{h}_b(t=T)=0$ as well as $\mathbf{h}_b(t=-\infty)=0$. Note the following definitions used in the integrated back-propagated field equations: $\mathbf{e}_b^{DC} = \int_{-\infty}^{T} dt\,\mathbf{e}_b$ and $\mathbf{h}_b^{DC} = \int_{-\infty}^{T} dt\,\mathbf{h}_b$. Inspection of the integrated back-propagated electric field shows that it can be obtained from the gradient of a scalar potential because $\nabla \mathrm{x}\mathbf{e}_b^{DC} = 0$. Thus, we may set $\nabla\theta_b = \mathbf{e}_b^{DC}$ and apply the divergence operator in equation (B20) and then solve

$$\nabla\cdot\sigma\nabla\theta_b = -\nabla\cdot\sum_i \int_0^T dt\;\frac{\delta \mathbf{e}^o(\mathbf{r}_i,t)}{t}\,\delta(\mathbf{r}-\mathbf{r}_i). \tag{B22}$$

Hence the gradient in equation (B17) is computed by using the back propagation equations (B15) and (B16) in order to determine $\mathbf{e}_b(\mathbf{r}',t'|\,\delta\mathbf{e}^o)$ and $\mathbf{h}_b(\mathbf{r}',t'|\,\delta\mathbf{e}^o)$ over the time range *T* to *0,* as well as solving Possion's equation (equation (B22)) to obtain $\mathbf{e}_b^{DC}(\mathbf{r}'|\,\delta\mathbf{e}^o)$.

For numerical accuracy, we prefer to express the gradient in equation (B17) as

$$\gamma_\sigma^e(\mathbf{r}') = \int_0^T dt'\, \mathbf{e}(\mathbf{r}',t') \cdot \mathbf{e}_b(\mathbf{r}',t'|\,\delta\mathbf{e}^o) - \mathbf{e}_{DC}(\mathbf{r}') \cdot \int_0^T dt'\, \mathbf{e}_b(\mathbf{r}',t'|\,\delta\mathbf{e}^o) + \mathbf{e}_{DC}(\mathbf{r}') \cdot \mathbf{e}_b^{DC}(\mathbf{r}'|\,\delta\mathbf{e}^o). \quad \text{(B23)}$$

If equation (B23) is used to evaluate the gradient, it is also necessary to integrate the back-propagated electric field, $\int_0^T dt'\, \mathbf{e}_b(\mathbf{r}',t'|\,\delta\mathbf{e}^o)$. This integral can easily be calculated as a byproduct during back-propagation of the electric field. We note that it is also possible to eliminate this integration by expressing equation (B23) as

$$\gamma_\sigma^e(\mathbf{r}') = -\int_0^T dt'\, \mathbf{e}^{on}(\mathbf{r}',t') \cdot \mathbf{e}_b(\mathbf{r}',t'|\,\delta\mathbf{e}^o) + \mathbf{e}_{DC}(\mathbf{r}') \cdot \mathbf{e}_b^{DC}(\mathbf{r}'|\,\delta\mathbf{e}^o)\ . \quad \text{(B24)}$$

Here, $\mathbf{e}^{on}(\mathbf{r}',t') = \mathbf{e}_{DC}(\mathbf{r}') - \mathbf{e}(\mathbf{r}',t')$ is the corresponding turn-on waveform, which is causal. Nevertheless, equation (B23) is favored over equation (B24) because subtractive cancellation could lead to a loss of accuracy in $\mathbf{e}^{on}(\mathbf{r}',t')$ at early times. We also note that equation (B23) reverts back to the causal form when $\mathbf{e}_{DC}(\mathbf{r}')$ is set to zero.

APPENDIX C

GRADIENT SPECIFICATION FOR VOLTAGE TYPE (-db/dt) DATA

Differentiating equations (B4) and (B5) with respect to time yields

$$\sigma \partial \delta \mathbf{e} / \partial t - \nabla \mathrm{x} \partial \delta \mathbf{h} / \partial t = -\delta \sigma \, \partial \mathbf{e} / \partial t \tag{C1}$$

$$\nabla \mathrm{x} \partial \delta \mathbf{e} / \partial t + \mu \, \partial \{ \partial \delta \mathbf{h} / \partial t \} / \partial t = -\delta \mu \frac{\partial^2}{\partial t^2} \mathbf{h}. \tag{C2}$$

and thus the perturbed time derivative of the magnetic field satisfies

$$\begin{aligned} \partial \delta \mathbf{h}(\mathbf{r}_i, t) / \partial t &= \int_{v'} \int_0^t \mathbf{G}_{21}(\mathbf{r}_i, t \mid \mathbf{r}', t') \frac{\partial \mathbf{e}(\mathbf{r}', t')}{\partial t'} \delta \sigma(\mathbf{r}') dt' d\mathbf{r}' \\ &+ \int_{v'} \int_0^t \frac{\mathbf{G}_{22}(\mathbf{r}_i, t \mid \mathbf{r}', t')}{\mu(\mathbf{r}')} \frac{\partial^2 \mathbf{h}(\mathbf{r}', t')}{\partial t'^2} \delta \mu(\mathbf{r}') dt' d\mathbf{r}' \end{aligned} \tag{C3}$$

The temporal integrations begin at time zero because the incident electric and magnetic fields are at steady state for $t<0$. The perturbed voltage follows immediately by scaling equation (C3) by $-\mu(\mathbf{r}_i)$. Thus

$$\begin{aligned} \delta \mathbf{u}(\mathbf{r}_i, t) &= \int_{v'} \int_0^t -\mu(\mathbf{r}_i) \mathbf{G}_{21}(\mathbf{r}_i, t \mid \mathbf{r}', t') \frac{\partial \mathbf{e}(\mathbf{r}', t')}{\partial t'} \delta \sigma(\mathbf{r}') dt' d\mathbf{r}' \\ &+ \int_{v'} \int_0^t -\frac{\mu(\mathbf{r}_i)}{\mu(\mathbf{r}')} \mathbf{G}_{22}(\mathbf{r}_i, t \mid \mathbf{r}', t') \frac{\partial^2 \mathbf{h}(\mathbf{r}', t')}{\partial t'^2} \delta \mu(\mathbf{r}') dt' d\mathbf{r}' \end{aligned} \tag{C4}$$

where $\delta \mathbf{u}(\mathbf{r}_i, t) = -\mu(\mathbf{r}_i) \delta \mathbf{h}(\mathbf{r}_i, t) / \partial t$. When the first term in equation (C4) is integrated by parts involving the integration variable *t'*, we find

$$\delta\mathbf{u}(\mathbf{r}_i,t)=\int_{v'}\int_0^t -\mu(\mathbf{r}_i)\,\frac{\partial\mathbf{G}_{21}(\mathbf{r}_i,t\,|\,\mathbf{r}',t')}{\partial t}\{\mathbf{e}(\mathbf{r}',t')-\mathbf{e}_{DC}(\mathbf{r}')\}\delta\sigma(\mathbf{r}')dt'd\mathbf{r}'$$
$$+\int_{v'}\int_0^t -\frac{\mu(\mathbf{r}_i)}{\mu(\mathbf{r}')}\mathbf{G}_{22}(\mathbf{r}_i,t\,|\,\mathbf{r}',t')\,\frac{\partial^2\mathbf{h}(\mathbf{r}',t')}{\partial t'^2}\delta\mu(\mathbf{r}')dt'd\mathbf{r}' \quad , \qquad \text{(C5)}$$

where the identity $\frac{\partial}{\partial t'}\mathbf{G}_{21}=-\frac{\partial}{\partial t}\mathbf{G}_{21}$ has been employed. We now follow a similar development discussed in Appendix B for electric field data. The voltage gradients for the conductivity and magnetic permeability are first written as

$$\gamma_\sigma^u(\mathbf{r}')=\sum_i\int_0^T dt\,\frac{\delta\mathbf{u}^o(\mathbf{r}_i,t)}{t}\int_0^t dt'\,\mu(\mathbf{r}_i)\frac{\partial\mathbf{G}_{21}(\mathbf{r}_i,t\,|\,\mathbf{r}',t')}{\partial t}\{\mathbf{e}(\mathbf{r}',t')-\mathbf{e}_{DC}(\mathbf{r}')\} \qquad \text{(C6)}$$

and

$$\gamma_\mu^u(\mathbf{r}')=\sum_i\int_0^T dt\,\frac{\delta\mathbf{u}^o(\mathbf{r}_i,t)}{t}\int_0^t dt'\frac{\mu(\mathbf{r}_i)}{\mu(\mathbf{r}')}\mathbf{G}_{22}(\mathbf{r}_i,t\,|\,\mathbf{r}',t')\frac{\partial^2\mathbf{h}(\mathbf{r}',t')}{\partial t'^2}. \qquad \text{(C7)}$$

Next, using reciprocity relations found in equations (A15) and (A17), which involve adjoint Dyadic Green's functions, we express the gradients in the more computationally efficient forms, where

$$\begin{aligned}\gamma_\sigma^u(\mathbf{r}')&=\sum_i\int_0^T dt\,\frac{\delta\mathbf{u}^o(\mathbf{r}_i,t)}{t}\int_0^t dt'\,\mu(\mathbf{r}_i)\frac{\partial\mathbf{G}_{21}(\mathbf{r}_i,t\,|\,\mathbf{r}',t')}{\partial t}\{\mathbf{e}(\mathbf{r}',t')-\mathbf{e}_{DC}(\mathbf{r}')\}\\
&=\sum_i\int_0^T dt'\int_{t'}^T\frac{\delta\mathbf{u}^o(\mathbf{r}_i,t)}{t}\mu(\mathbf{r}_i)\frac{\partial\mathbf{G}_{21}(\mathbf{r}_i,t\,|\,\mathbf{r}',t')}{\partial t}\{\mathbf{e}(\mathbf{r}',t')-\mathbf{e}_{DC}(\mathbf{r}')\}dt\\
&=-\sum_i\int_0^T dt'\int_{t'}^T\{\mathbf{e}(\mathbf{r}',t')-\mathbf{e}_{DC}(\mathbf{r}')\}\mathbf{G}_{12}^{+}(\mathbf{r}',t'|\,\mathbf{r}_i,t)\,\frac{\delta\mathbf{u}^o(\mathbf{r}_i,t)}{t}dt\\
&=\int_0^T dt'\,\{\mathbf{e}(\mathbf{r}',t')-\mathbf{e}_{DC}(\mathbf{r}')\}\cdot\sum_i\int_T^{t'}dt\;\mathbf{G}_{12}^{+}(\mathbf{r}',t'|\,\mathbf{r}_i,t)\,\frac{\delta\mathbf{u}^o(\mathbf{r}_i,t)}{t}\\
&=\int_0^T dt'\;\mathbf{e}(\mathbf{r}',t')\cdot\mathbf{e}_b(\mathbf{r}',t'|\,\delta\mathbf{u}^o)-\mathbf{e}_{DC}(\mathbf{r}')\cdot\int_0^T dt'\;\mathbf{e}_b(\mathbf{r}',t'|\,\delta\mathbf{u}^o)\end{aligned} \qquad \text{(C8)}$$

and

$$
\begin{aligned}
\gamma_{\mu}^{u}(\mathbf{r}') &= \sum_i \int_0^T dt\ \frac{\delta\mathbf{u}^o(\mathbf{r}_i,t)}{t} \int_0^t dt' \frac{\mu(\mathbf{r}_i)}{\mu(\mathbf{r}')} \mathbf{G}_{22}(\mathbf{r}_i,t\,|\,\mathbf{r}',t') \frac{\partial^2\mathbf{h}(\mathbf{r}',t')}{\partial t'^2} \\
&= \sum_i \int_0^T dt' \int_{t'}^T \frac{\delta\mathbf{u}^o(\mathbf{r}_i,t)}{t} \frac{\mu(\mathbf{r}_i)}{\mu(\mathbf{r}')} \mathbf{G}_{22}(\mathbf{r}_i,t\,|\,\mathbf{r}',t') \frac{\partial^2\mathbf{h}(\mathbf{r}',t')}{\partial t'^2} dt \\
&= \sum_i \int_0^T dt' \int_{t'}^T \frac{\partial^2\mathbf{h}(\mathbf{r}',t')}{\partial t'^2} \mathbf{G}_{22}^{+}(\mathbf{r}',t'|\,\mathbf{r}_i,t) \frac{\delta\mathbf{u}^o(\mathbf{r}_i,t)}{t} dt \\
&= -\int_0^T dt' \frac{\partial^2\mathbf{h}(\mathbf{r}',t')}{\partial t'^2} \cdot \sum_i \int_T^{t'} dt\ \mathbf{G}_{22}^{+}(\mathbf{r}',t'|\,\mathbf{r}_i,t) \frac{\delta\mathbf{u}^o(\mathbf{r}_i,t)}{t} \\
&= -\int_0^T dt' \frac{\partial^2}{\partial t'^2}\mathbf{h}(\mathbf{r}',t') \cdot \mathbf{h}_b(\mathbf{r}',t'|\,\delta\mathbf{u}^o) \\
&= \int_0^T dt' \frac{\partial\mathbf{h}(\mathbf{r}',t')}{\partial t'} \cdot \frac{\partial\mathbf{h}_b(\mathbf{r}',t'|\,\delta\mathbf{u}^o)}{\partial t'},
\end{aligned}
\tag{C9}
$$

where we have assumed that $\frac{\partial\mathbf{h}(\mathbf{r}',0)}{\partial t'}=0$ and $\mathbf{h}_b(\mathbf{r}',T\,|\,\delta\mathbf{u}^o)=0.$ In equations (C8) and (C9) we have defined the following back-propagated electric and magnetic fields,

$$
\mathbf{e}_b(\mathbf{r}',t'|\,\delta\mathbf{u}^o) = \sum_i \int_T^{t'} dt\, \mathbf{G}_{12}^{+}(\mathbf{r}',t'|\,\mathbf{r}_i,t) \frac{\delta\mathbf{u}^o(\mathbf{r}_i,t)}{t} \tag{C10}
$$

and

$$
\mathbf{h}_b(\mathbf{r}',t'|\,\delta\mathbf{u}^o) = \sum_i \int_T^{t'} dt\, \mathbf{G}_{22}^{+}(\mathbf{r}',t'|\,\mathbf{r}_i,t) \frac{\delta\mathbf{u}^o(\mathbf{r}_i,t)}{t}. \tag{C11}
$$

Using equations (A11) and (A12), the back-propagated fields in equations (C10) and (C11) can be shown to satisfy the adjoint Maxwell equations,

$$
\sigma\mathbf{e}_b + \nabla\mathrm{x}\mathbf{h}_b = 0 \tag{C12}
$$

$$
-\nabla\mathrm{x}\mathbf{e}_b - \mu\,\partial\mathbf{h}_b/\partial t = -\sum_i \mu(\mathbf{r}_i) \frac{\delta\mathbf{u}^o(\mathbf{r}_i,t)}{t} \delta(\mathbf{r}-\mathbf{r}_i) \tag{C13}
$$

over the time range T to 0 in reverse time.

APPENDIX D

GRADIENT SPECIFICATION FOR MAGNETIC FIELD DATA

The perturbed magnetic field arising from a turn off of a steady state source current at time zero is related to the corresponding field arising from a turn on of the source current, by the relationship $\delta\mathbf{h}^{off}(\mathbf{r}_i,t) = \delta\mathbf{h}_{DC}(\mathbf{r}_i) - \delta\mathbf{h}^{on}(\mathbf{r}_i,t)$, where $\delta\mathbf{h}_{DC}(\mathbf{r}_i)$ is the perturbed DC field, both in conductivity and permeability, present before shutoff. Thus we can express the perturbed field, $\delta\mathbf{h}^{off}(\mathbf{r}_i,t)$, as

$$\delta\mathbf{h}^{off}(\mathbf{r}_i,t) = \delta\mathbf{h}^{\sigma}_{DC}(\mathbf{r}_i) - \int_{v'} d\mathbf{r}' \int_0^t \mathbf{G}_{21}(\mathbf{r}_i,t \mid \mathbf{r}',t')\mathbf{e}^{on}(\mathbf{r}',t')\delta\sigma(\mathbf{r}')dt' \qquad \text{(D1)}$$

$$+ \delta\mathbf{h}^{\mu}_{DC}(\mathbf{r}_i) - \int_{v'} d\mathbf{r}' \int_0^t \frac{\mathbf{G}_{22}(\mathbf{r}_i,t \mid \mathbf{r}',t')}{\mu(\mathbf{r}')} \frac{\partial\mathbf{h}^{on}(\mathbf{r}',t')}{\partial t'}\delta\mu(\mathbf{r}')dt'.$$

The vector functions, $\delta\mathbf{h}^{\sigma}_{DC}(\mathbf{r}_i)$ and $\delta\mathbf{h}^{\mu}_{DC}(\mathbf{r}_i)$, represent components of the perturbed DC magnetic field, $\delta\mathbf{h}_{DC}(\mathbf{r}_i)$, that arise from electrical conductivity and magnetic permeability variations within the earth; these quantities will be specified shortly. However, it is important to observe now that $\delta\mathbf{h}^{\mu}_{DC}(\mathbf{r}_i)$ will be in the null-space of the perturbation equations (B4) and (B5) because it arises at steady state and is curl-free. It must be curl free because this field has no influence on the electric fields at DC or steady state; the DC electric field is sensitive only to variations in electric conductivity. Furthermore, because the field is curl free it can also be represented by a gradient of a scalar potential.

Because $\mathbf{e}^{on}(\mathbf{r}',t') = \mathbf{e}_{DC}(\mathbf{r}') - \mathbf{e}^{off}(\mathbf{r}',t')$ and $\frac{\partial}{\partial t'}\mathbf{h}^{on}(\mathbf{r}',t') = -\frac{\partial}{\partial t'}\mathbf{h}^{off}(\mathbf{r}',t')$, we can also express equation (D1) as

$$\delta\mathbf{h}^{off}(\mathbf{r}_i,t)=\delta\mathbf{h}^{\sigma}_{DC}(\mathbf{r}_i)+\int_{v'}d\mathbf{r}'\int_0^t\mathbf{G}_{21}(\mathbf{r}_i,t\,|\,\mathbf{r}',t')\{\mathbf{e}^{off}(\mathbf{r}',t')-\mathbf{e}_{DC}(\mathbf{r}')\}\delta\sigma(\mathbf{r}')dt'$$
$$+\delta\mathbf{h}^{\mu}_{DC}(\mathbf{r}_i)+\int_{v'}d\mathbf{r}'\int_0^t\frac{\mathbf{G}_{22}(\mathbf{r}_i,t\,|\,\mathbf{r}',t')}{\mu(\mathbf{r}')}\frac{\partial\mathbf{h}^{off}(\mathbf{r}',t')}{\partial t'}\delta\mu(\mathbf{r}')dt'\ . \qquad \text{(D2)}$$

Hence, using equations (B1), (B2) and (B3) for magnetic field data, the gradients can be expressed for conductivity as

$$\gamma^h_\sigma(\mathbf{r}')=-\sum_i\int_0^T dt\frac{\delta\mathbf{h}^o(\mathbf{r}_i,t)}{t}\delta\mathbf{h}^{\sigma}_{DC}(\mathbf{r}_i,\mathbf{r}')$$
$$-\sum_i\int_0^T dt\frac{\delta\mathbf{h}^o(\mathbf{r}_i,t)}{t}\int_0^t dt'\mathbf{G}_{21}(\mathbf{r}_i,t\,|\,\mathbf{r}',t')\{\mathbf{e}(\mathbf{r}',t')-\mathbf{e}_{DC}(\mathbf{r}')\} \qquad \text{(D3)}$$

and for the magnetic permeability as

$$\gamma^h_\mu(\mathbf{r}')=-\sum_i\int_0^T dt\frac{\delta\mathbf{h}^o(\mathbf{r}_i,t)}{t}\delta\mathbf{h}^{\mu}_{DC}(\mathbf{r}_i,\mathbf{r}')$$
$$-\sum_i\int_0^T dt\frac{\delta\mathbf{h}^o(\mathbf{r}_i,t)}{t}\int_0^t dt'\frac{\mathbf{G}_{22}(\mathbf{r}_i,t\,|\,\mathbf{r}',t')}{\mu(\mathbf{r}')}\frac{\partial\mathbf{h}(\mathbf{r}',t')}{\partial t'}, \qquad \text{(D4)}$$

where we have dropped the *'off'* notation going forward and we have now included the dependence upon the image point $\mathbf{r}'$ in the vector functions $\delta\mathbf{h}^{\sigma}_{DC}$ and $\delta\mathbf{h}^{\mu}_{DC}$; these functions are to be specified below.

The gradients in equations (D3) and (D4) are conveniently split into two parts,

$${}^1\gamma^h_\sigma(\mathbf{r}')=-\sum_i\int_0^T dt\frac{\delta\mathbf{h}^o(\mathbf{r}_i,t)}{t}\delta\mathbf{h}^{\sigma}_{DC}(\mathbf{r}_i,\mathbf{r}') \qquad \text{(D5)}$$

$${}^2\gamma^h_\sigma(\mathbf{r}')=-\sum_i\int_0^T dt\frac{\delta\mathbf{h}^o(\mathbf{r}_i,t)}{t}\int_0^t dt'\mathbf{G}_{21}(\mathbf{r}_i,t\,|\,\mathbf{r}',t')\{\mathbf{e}(\mathbf{r}',t')-\mathbf{e}_{DC}(\mathbf{r}')\} \qquad \text{(D6)}$$

$${}^1\gamma^h_\mu(\mathbf{r}')=-\sum_i\int_0^T dt\frac{\delta\mathbf{h}^o(\mathbf{r}_i,t)}{t}\delta\mathbf{h}^{\mu}_{DC}(\mathbf{r}_i,\mathbf{r}') \qquad \text{(D7)}$$

and

$${}^2\gamma^h_\mu(\mathbf{r}')=-\sum_i\int_0^T dt\frac{\delta\mathbf{h}^o(\mathbf{r}_i,t)}{t}\int_0^t dt'\frac{\mathbf{G}_{22}(\mathbf{r}_i,t\,|\,\mathbf{r}',t')}{\mu(\mathbf{r}')}\frac{\partial\mathbf{h}(\mathbf{r}',t')}{\partial t'}\ . \qquad \text{(D8)}$$

Using the reciprocity relationship in equation (A18) we modify equation (D6) as

$$
\begin{aligned}
{}^{2}\gamma_{\sigma}^{h}(\mathbf{r}') &= -\sum_i \int_0^T dt\ \frac{\delta\mathbf{h}^o(\mathbf{r}_i,t)}{t} \int_0^t dt'\mathbf{G}_{21}(\mathbf{r}_i,t\,|\,\mathbf{r}',t')\,\{\mathbf{e}(\mathbf{r}',t')-\mathbf{e}_{DC}(\mathbf{r}')\} \\
&= -\sum_i \int_0^T dt' \int_{t'}^T \frac{\delta\mathbf{h}^o(\mathbf{r}_i,t)}{t}\mathbf{G}_{21}(\mathbf{r}_i,t\,|\,\mathbf{r}',t')\ \{\mathbf{e}(\mathbf{r}',t')-\mathbf{e}_{DC}(\mathbf{r}')\}\,dt \\
&= -\sum_i \int_0^T dt' \int_{t'}^T \ \{\mathbf{e}(\mathbf{r}',t')-\mathbf{e}_{DC}(\mathbf{r}')\}\ \frac{{}^{step}\mathbf{G}_{12}^{+}(\mathbf{r}',t'|\,\mathbf{r}_i,t)}{\mu(\mathbf{r}_i)}\,\frac{\delta\mathbf{h}^o(\mathbf{r}_i,t)}{t}\,dt \\
&= \int_0^T dt'\ \ \{\mathbf{e}(\mathbf{r}',t')-\mathbf{e}_{DC}(\mathbf{r}')\}\cdot\sum_i\ \int_T^{t'} dt\ \frac{{}^{step}\mathbf{G}_{12}^{+}(\mathbf{r}',t'|\,\mathbf{r}_i,t)}{\mu(\mathbf{r}_i)}\,\frac{\delta\mathbf{h}^o(\mathbf{r}_i,t)}{t} \\
&= \int_0^T dt'\ \mathbf{e}(\mathbf{r}',t')\cdot\mathbf{e}_b^{step}(\mathbf{r}',t'|\,\delta\mathbf{h}^o)-\mathbf{e}_{DC}(\mathbf{r}')\cdot\int_0^T dt'\ \mathbf{e}_b^{step}(\mathbf{r}',t'|\,\delta\mathbf{h}^o)
\end{aligned}
\tag{D9}
$$

where

$$
\mathbf{e}_b^{step}(\mathbf{r}',t'|\,\delta\mathbf{h}^o)=\sum_i\ \int_T^{t'} dt\ \frac{{}^{step}\mathbf{G}_{12}^{+}(\mathbf{r}',t'|\,\mathbf{r}_i,t)}{\mu(\mathbf{r}_i)}\,\frac{\delta\mathbf{h}^o(\mathbf{r}_i,t)}{t}\,. \tag{D10}
$$

Differentiating equation (D10) with respect to t' it is easy to show that

$$
\frac{\partial\mathbf{e}_b^{step}(\mathbf{r}',t'|\,\delta\mathbf{h}^o)}{\partial t'}=\mathbf{e}_b(\mathbf{r}',t'|\,\delta\mathbf{h}^o) \tag{D11}
$$

where

$$
\mathbf{e}_b(\mathbf{r}',t'|\,\delta\mathbf{h}^o)=\sum_i\ \int_T^{t'} dt\ \ \frac{\mathbf{G}_{12}^{+}(\mathbf{r}',t'|\,\mathbf{r}_i,t)}{\mu(\mathbf{r}_i)}\,\frac{\delta\mathbf{h}^o(\mathbf{r}_i,t)}{t}\,. \tag{D12}
$$

When we consider equation (D8) and use equation (A17), along with similar series of steps used for the conductivity gradient, we have,

$$
\begin{aligned}
{}^{2}\gamma_{\mu}^{h}(\mathbf{r}') &= -\sum_i \int_0^T dt\ \frac{\delta\mathbf{h}^o(\mathbf{r}_i,t)}{t}\int_0^t dt'\frac{\mathbf{G}_{22}(\mathbf{r}_i,t\,|\,\mathbf{r}',t')}{\mu(\mathbf{r}')}\,\frac{\partial}{\partial t'}\mathbf{h}(\mathbf{r}',t') \\
&= -\sum_i \int_0^T dt' \int_{t'}^T \frac{\delta\mathbf{h}^o(\mathbf{r}_i,t)}{t}\,\frac{\mathbf{G}_{22}(\mathbf{r}_i,t\,|\,\mathbf{r}',t')}{\mu(\mathbf{r}')}\,\frac{\partial}{\partial t'}\mathbf{h}(\mathbf{r}',t')\,dt \\
&= -\sum_i \int_0^T dt' \int_{t'}^T \frac{\partial}{\partial t'}\mathbf{h}(\mathbf{r}',t')\ \frac{\mathbf{G}_{22}^{+}(\mathbf{r}',t'|\,\mathbf{r}_i,t)}{\mu(\mathbf{r}_i)}\,\frac{\delta\mathbf{h}^o(\mathbf{r}_i,t)}{t}\,dt
\end{aligned}
$$

$$= \int_0^T dt' \, \frac{\partial}{\partial t'} \mathbf{h}(\mathbf{r}', t') \cdot \sum_i \int_T^{t'} dt \, \frac{\mathbf{G}_{22}^{+}(\mathbf{r}', t' | \mathbf{r}_i, t)}{\mu(\mathbf{r}_i)} \frac{\delta \mathbf{h}^o(\mathbf{r}_i, t)}{t}$$

$$= \int_0^T dt' \, \frac{\partial}{\partial t'} \mathbf{h}(\mathbf{r}', t') \cdot \mathbf{h}_b(\mathbf{r}', t' | \delta \mathbf{h}^o) \,. \tag{D13}$$

where

$$\mathbf{h}_b(\mathbf{r}', t' | \delta \mathbf{h}^o) = \sum_i \int_T^{t'} dt \, \frac{\mathbf{G}_{22}^{+}(\mathbf{r}_i, t | \mathbf{r}', t')}{\mu(\mathbf{r}_i)} \frac{\delta \mathbf{h}^o(\mathbf{r}_i, t)}{t} \,. \tag{D14}$$

It is now straightforward to show, by using equations (A11) and (A12) that the back-propagated electric and magnetic fields in equations (D12) and (D14) satisfy the adjoint Maxwell equations in reverse time, from time T to 0,

$$\sigma \mathbf{e}_b + \nabla \mathrm{x} \mathbf{h}_b = 0 \tag{D15}$$

$$-\nabla \mathrm{x} \mathbf{e}_b - \mu \partial \mathbf{h}_b / \partial t = -\sum_i \frac{\delta \mathbf{h}^o(\mathbf{r}_i, t)}{t} \, \delta(\mathbf{r} - \mathbf{r}_i) \,. \tag{D16}$$

We now treat the DC components of the gradient (equations (D5) and (D7)). For the DC conductivity gradient, the perturbed Maxwell equations (B4) and (B5) at DC are expressed as

$$\sigma \delta \mathbf{e}_{DC}^{\sigma} - \nabla \mathrm{x} \delta \mathbf{h}_{DC}^{\sigma} = -\delta \sigma \, \mathbf{e}_{DC} \tag{D17}$$

$$\nabla \mathrm{x} \delta \mathbf{e}_{DC}^{\sigma} = 0. \tag{D18}$$

Now the perturbed magnetic field can be determined from the DC electric field, where

$$\nabla \mathrm{x} \frac{1}{\sigma} \nabla \mathrm{x} \delta \mathbf{h}_{DC}^{\sigma} = \nabla \mathrm{x} \frac{\delta \sigma}{\sigma} \mathbf{e}_{DC} \,. \tag{D19}$$

Solution to equation (D19) is formally written as

$$\delta \mathbf{h}^{\sigma}_{DC}(\mathbf{r}) = \int_{v'} \mathbf{G}(\mathbf{r},\mathbf{r}') \nabla' \mathrm{x} \frac{\delta\sigma(\mathbf{r}')}{\sigma(\mathbf{r}')} \mathbf{e}_{DC}(\mathbf{r}')\, d\mathbf{r}' \tag{D20}$$

where the tensor Green's function, $\mathbf{G}(\mathbf{r},\mathbf{r}')$, satisfies the following equation,

$$\nabla \mathrm{x} \frac{1}{\sigma} \nabla \mathrm{x} \mathbf{G} = -\zeta(\mathbf{r} - \mathbf{r}'). \tag{D21}$$

Because of the symmetric operator in equation (D21) we deduce the following reciprocity relationship

$$\tilde{\mathbf{G}}(\mathbf{r},\mathbf{r}') = \mathbf{G}(\mathbf{r}',\mathbf{r}), \tag{D22}$$

where ~ denotes transposition of a dyadic. Abstracting from equation (B1), the perturbation in the cost functional related to the DC part of the problem for magnetic field data is expressed as

$$\delta \vartheta_{DC}(\sigma) = -\sum_i \int_0^T dt \ \frac{\delta \mathbf{h}^{o}(\mathbf{r}_i,t)}{t} \cdot \delta \mathbf{h}^{\sigma}_{DC}(\mathbf{r}_i). \tag{D23}$$

Substituting equation (D20) into (D23) produces

$$\delta \vartheta_{DC}(\sigma) = -\int_{v'} d\mathbf{r}' \sum_i \int_0^T dt \frac{\delta \mathbf{h}^{o}(\mathbf{r}_i,t)}{t} \mathbf{G}(\mathbf{r}_i,\mathbf{r}') \nabla' \mathrm{x} \frac{\delta\sigma(\mathbf{r}')}{\sigma(\mathbf{r}')} \mathbf{e}_{DC}(\mathbf{r}'). \tag{D24}$$

Taking the transpose of equation (D24), noting equation (D22), allows one to write equation (D24) as

$$\delta \vartheta_{DC}(\sigma) = -\int_{v'} d\mathbf{r}' \sum_i \nabla' \mathrm{x} \frac{\delta\sigma(\mathbf{r}')}{\sigma(\mathbf{r}')} \mathbf{e}_{DC}(\mathbf{r}') \mathbf{G}(\mathbf{r}',\mathbf{r}_i) \int_0^T dt \frac{\delta \mathbf{h}^{o}(\mathbf{r}_i,t)}{t}. \tag{D25}$$

Next using the dyadic identity, that can be found in Tai (1990),

$$\begin{aligned} \nabla' \mathrm{x} \frac{\delta\sigma(\mathbf{r}')}{\sigma(\mathbf{r}')} \mathbf{e}_{DC}(\mathbf{r}') \mathbf{G}(\mathbf{r}',\mathbf{r}_i) &= \nabla' \cdot \{ \frac{\delta\sigma(\mathbf{r}')}{\sigma(\mathbf{r}')} \mathbf{e}_{DC}(\mathbf{r}') \mathrm{x} \mathbf{G}(\mathbf{r}',\mathbf{r}_i) \} \\ + \frac{\delta\sigma(\mathbf{r}')}{\sigma(\mathbf{r}')} \mathbf{e}_{DC}(\mathbf{r}') &\cdot (\nabla' \mathrm{x} \mathbf{G}(\mathbf{r}',\mathbf{r}_i)) \end{aligned} \tag{D26}$$

and the divergence theorem for tensors (see Chew (1990)), we can express equation (D25) as

$$\begin{aligned}\delta\vartheta_{DC}(\sigma) = &-\int_{v'} d\mathbf{r}' \sum_i \frac{\delta\sigma(\mathbf{r}')}{\sigma(\mathbf{r}')} \mathbf{e}_{DC}(\mathbf{r}') \nabla' \mathrm{x} \mathbf{G}(\mathbf{r}', \mathbf{r}_i) \int_0^T dt \frac{\delta \mathbf{h}^o(\mathbf{r}_i, t)}{t} \\ &- \oiint d\mathbf{r}' \hat{\mathbf{n}} \cdot \{ \frac{\delta\sigma(\mathbf{r}')}{\sigma(\mathbf{r}')} \mathbf{e}_{DC}(\mathbf{r}') \mathrm{x} \mathbf{G}(\mathbf{r}', \mathbf{r}_i) \} \int_0^T dt \frac{\delta \mathbf{h}^o(\mathbf{r}_i, t)}{t}\end{aligned} . \tag{D27}$$

The last term in equation (D27) vanishes as the points $\mathbf{r}'$ on the enclosed surface tend to infinity, with respect to interior points inside the volume, including all sources of the fields and measurement points $\mathbf{r}_i$. Using this fact, along with equations (B2) and (B3) we finally express the DC gradient term in equation (D5) as

$${}^1\gamma_\sigma^h(\mathbf{r}') = -\sum_i \frac{1}{\sigma(\mathbf{r}')} \mathbf{e}_{DC}(\mathbf{r}') \nabla' \mathrm{x} \mathbf{G}(\mathbf{r}', \mathbf{r}_i) \int_0^T dt \frac{\delta \mathbf{h}^o(\mathbf{r}_i, t)}{t}, \tag{D28}$$

where

$$\delta \mathbf{h}_{DC}^{\sigma}(\mathbf{r}_i, \mathbf{r}') = \frac{1}{\sigma(\mathbf{r}')} \mathbf{e}_{DC}(\mathbf{r}') \nabla' \mathrm{x} \mathbf{G}(\mathbf{r}', \mathbf{r}_i) . \tag{D29}$$

At this point we define a DC back propagated electric field

$$\mathbf{e}_b^{DC}(\mathbf{r}' | \delta \mathbf{h}^o) = -\sum_i \frac{1}{\sigma(\mathbf{r}')} \nabla' \mathrm{x} \mathbf{G}(\mathbf{r}', \mathbf{r}_i) \int_0^T dt \frac{\delta \mathbf{h}^o(\mathbf{r}_i, t)}{t}, \tag{D30}$$

such that

$${}^1\gamma_\sigma^h(\mathbf{r}') = \mathbf{e}_{DC}(\mathbf{r}') \cdot \mathbf{e}_b^{DC}(\mathbf{r}' | \delta \mathbf{h}^o) \tag{D31}$$

where from equation (D21) we observe that this back propagated field satisfies

$$\nabla \mathrm{x} \mathbf{e}_b^{DC} = \sum_i \int_0^T dt \frac{\delta \mathbf{h}^o(\mathbf{r}_i, t)}{t} \delta(\mathbf{r} - \mathbf{r}_i), \tag{D32}$$

which also can be derived by integrating equation (D16) over the time range $\{T,-\infty\}$, and setting $\mathbf{e}_b^{DC} = \int_{-\infty}^{T} dt\, \mathbf{e}_b$, given the $\mathbf{h}_b(t=T)=0$ and $\mathbf{h}_b(t=-\infty)=0$. Because the magnetic field data, that is sensitive to electrical conductivity, is divergence free (this can be directly seen by applying the divergence operator to equation (D32)) we take the curl of equation (D32),

$$\nabla \mathrm{x} \nabla \mathrm{x} \mathbf{e}_b^{DC} = \nabla \mathrm{x} \sum_i \int_0^T dt\, \frac{\delta \mathbf{h}^o(\mathbf{r}_i, t)}{t} \delta(\mathbf{r} - \mathbf{r}_i). \tag{D33}$$

Equation (D33) has a nontrivial null space given by the vector fields described by the gradient of a scalar potential. Hence special techniques are needed to deflate this null space out from $\mathbf{e}_b^{DC}(\mathbf{r}' | \delta \mathbf{h}^o)$. Methods of solution that accomplish this task can be found in Chan et al. (2002).

Next we now turn our attention to equation (D7). We first show that the perturbed DC magnetic field, $\delta \mathbf{h}_{DC}^{\mu}$ in equation (D1), satisfies,

$$\delta \mathbf{h}_{DC}^{\mu}(\mathbf{r}_i) = \int_{v'} \nabla g(\mathbf{r}_i, \mathbf{r}') \nabla' \cdot \mathbf{h}_{DC}(\mathbf{r}') \delta \mu(\mathbf{r}') d\mathbf{r}', \tag{D34}$$

where $g(\mathbf{r}_i, \mathbf{r}')$ is a scalar Green's function yet to be determined. Equation (D34) can be derived directly from the Maxwell equations using a perturbation analysis for magnetic permeability at steady state, where

$$\nabla \mathrm{x} \delta \mathbf{h}_{DC}^{\mu} = 0 \tag{D35}$$

and

$$\delta \mathbf{e}_{DC}^{\mu} = 0. \tag{D36}$$

Now we know $\mathbf{b}_{DC} = \mu \mathbf{h}_{DC}$ and $\mathbf{b}_{DC} + \delta \mathbf{b}^{\mu}_{DC} = (\mu + \delta\mu)(\mathbf{h}_{DC} + \delta \mathbf{h}^{\mu}_{DC})$. Because $\nabla \cdot \mathbf{b}_{DC} = 0$ and $\nabla \cdot (\mathbf{b}_{DC} + \delta \mathbf{b}^{\mu}_{DC}) = 0$, it therefore follows that $\nabla \cdot \delta \mathbf{b}^{\mu}_{DC} = 0$, where $\delta \mathbf{b}^{\mu}_{DC} = \mu \delta \mathbf{h} + \delta\mu \mathbf{h}^{\mu}_{DC} + \delta\mu \delta \mathbf{h}^{\mu}_{DC} \approx \mu \delta \mathbf{h}^{\mu}_{DC} + \delta\mu \mathbf{h}_{DC}$. Thus we set

$$0 = \nabla \cdot \mu \delta \mathbf{h}^{\mu}_{DC} + \nabla \cdot \delta\mu \, \mathbf{h}_{DC} . \tag{D37}$$

Next using the fact that $\nabla \mathrm{x} \delta \mathbf{h}^{\mu}_{DC} = 0$, we set $\delta \mathbf{h}^{\mu}_{DC} = \nabla \phi,$ and solve

$$\nabla \cdot \mu \nabla \phi = -\nabla \cdot \delta\mu \, \mathbf{h}_{DC}. \tag{D38}$$

The solution to the above Possion equation is formally expressed as

$$\phi(\mathbf{r}) = \int_{v'} g(\mathbf{r}, \mathbf{r}') \nabla' \cdot \mathbf{h}_{DC}(\mathbf{r}') \delta\mu(\mathbf{r}') d\mathbf{r}' \tag{D39}$$

and

$$\delta \mathbf{h}^{\mu}_{DC}(\mathbf{r}_i) = \int_{v'} \nabla g(\mathbf{r}_i, \mathbf{r}') \nabla' \cdot \mathbf{h}_{DC}(\mathbf{r}') \delta\mu(\mathbf{r}') d\mathbf{r}'. \tag{D40}$$

Here the scalar Green's function satisfies

$$\nabla \cdot \mu \nabla g = -\delta(\mathbf{r} - \mathbf{r}'). \tag{D41}$$

Abstracting again from equation (B1), where $\delta \vartheta_{DC}(\mu) = -\sum_i \int_0^T dt \, \frac{\delta \mathbf{h}^{o}(\mathbf{r}_i, t)}{t} \cdot \delta \mathbf{h}^{\mu}_{DC}(\mathbf{r}_i)$, we have

$$\delta \vartheta_{DC}(\mu) = -\int_v dv' \sum_i \int_0^T dt \frac{\delta \mathbf{h}^{o}(\mathbf{r}_i, t)}{t} \nabla g(\mathbf{r}_i, \mathbf{r}') \nabla' \cdot \mathbf{h}_{DC}(\mathbf{r}') \delta\mu(\mathbf{r}') . \tag{D42}$$

Next, using equations (B2), (B3) and (D42), we find

$$^{1}\gamma^{h}_{\mu}(\mathbf{r}') = -\sum_i \int_0^T dt \, \frac{\delta \mathbf{h}^{o}(\mathbf{r}_i, t)}{t} \nabla g(\mathbf{r}_i, \mathbf{r}') \nabla' \cdot \mathbf{h}_{DC}(\mathbf{r}'), \tag{D43}$$

where

$$\delta\mathbf{h}^{\mu}_{DC}(\mathbf{r}_i,\mathbf{r}') = \nabla g(\mathbf{r}_i,\mathbf{r}')\nabla'\cdot\mathbf{h}_{DC}(\mathbf{r}') \tag{D44}$$

in equation (D7). Because $g(\mathbf{r},\mathbf{r}') = g(\mathbf{r}',\mathbf{r})$ the following reciprocity relation can be shown to hold:

$$\mathbf{v}(\mathbf{r})\cdot\nabla g(\mathbf{r},\mathbf{r}')\nabla'\cdot\mathbf{u}(\mathbf{r}') = \mathbf{u}(\mathbf{r}')\cdot\nabla' g\ (\mathbf{r}',\mathbf{r})\nabla\cdot\mathbf{v}(\mathbf{r})\ . \tag{D45}$$

Here we note that the arbitrary vector, $\mathbf{v}(\mathbf{r})$, and scalar Greens function, $g(\mathbf{r},\mathbf{r}')$, sourced at $\mathbf{r}'$, vanish as $|\mathbf{r}|\to\infty$, where $\mathbf{r}'$ stays finite. Likewise the arbitrary vector, $\mathbf{u}(\mathbf{r}')$, and the Green's function $g(\mathbf{r}',\mathbf{r})$, sourced at $\mathbf{r}$, vanish as $|\mathbf{r}'|\to\infty$, with $\mathbf{r}$ finite. Thus the DC component of the gradient can be expressed point wise as

$${}^{1}\gamma^{h}_{\mu}(\mathbf{r}') = -\sum_i\int_0^T dt\,\mathbf{h}_{DC}(\mathbf{r}')\cdot\nabla' g(\mathbf{r}',\mathbf{r}_i)\nabla\cdot\frac{\delta\mathbf{h}^{o}(\mathbf{r}_i,t)}{t}. \tag{D46}$$

We find it convenient to define a DC back-propagated magnetic field

$$\mathbf{h}^{DC}_{b}(\mathbf{r}'|\,\delta\mathbf{h}^{o}) = -\sum_i\ \nabla' g(\mathbf{r}',\mathbf{r}_i)\nabla\cdot\int_0^T\ \frac{\delta\mathbf{h}^{o}(\mathbf{r}_i,t)}{t}dt. \tag{D47}$$

To effectively compute this back-propagated field, we multiply equation (D47) by the operator $\nabla'\cdot\mu(\mathbf{r}')$ to obtain

$$\nabla'\cdot\mu(\mathbf{r}')\mathbf{h}^{DC}_{b}(\mathbf{r}') = -\sum_i\nabla'\cdot\mu(\mathbf{r}')\nabla' g(\mathbf{r}',\mathbf{r}_i)\nabla\cdot\int_0^T\ \frac{\delta\mathbf{h}^{o}(\mathbf{r}_i,t)}{t}dt. \tag{D48}$$

Because $\nabla' x\mathbf{h}^{DC}_{b} = 0$, $\mathbf{h}^{DC}_{b}$ is determined from the gradient of a scalar potential. Using this fact along with equation (D41) we find that

$$\nabla'\cdot\mu(\mathbf{r}')\nabla'\phi_b(\mathbf{r}') = \nabla'\cdot\sum_i\ \int_0^T\ \frac{\delta\mathbf{h}^{o}(\mathbf{r}',t)}{t}dt\ \delta(\mathbf{r}'-\mathbf{r}_i), \tag{D49}$$

where

$$\mathbf{h}^{DC}_{b} = \nabla'\phi_b\,. \tag{D50}$$

Thus the DC component of the gradient in equation (D7) is compactly expressed as

$$^{1}\gamma_{\mu}^{h}(\mathbf{r}') = \mathbf{h}_{DC}(\mathbf{r}') \cdot \mathbf{h}_{b}^{DC}(\mathbf{r}' | \delta\mathbf{h}^{o}). \tag{D51}$$

Because the DC back-propagated magnetic field is curl free it cannot be obtained by integrating equation (D15) over the time range T to -∞, setting $\mathbf{h}_{b}^{DC} = \int_{-\infty}^{T} dt\, \mathbf{h}_{b}$, and then using (D16) to eliminate the back- propagated DC electric field. Instead, we see, it is determined from a projection of the magnetic field data errors that is curl free.

Combining equations (D9) and (D31) and equations (D13) and (D51) the gradients for electrical conductivity and magnetic permeability are finally expressed as

$$\begin{aligned}\gamma_{\sigma}^{h}(\mathbf{r}') = &\int_{0}^{T} dt'\, \mathbf{e}(\mathbf{r}', t') \cdot \mathbf{e}_{b}^{step}(\mathbf{r}', t' | \delta\mathbf{h}^{o}) - \mathbf{e}_{DC}(\mathbf{r}') \cdot \int_{0}^{T} dt'\, \mathbf{e}_{b}^{step}(\mathbf{r}', t' | \delta\mathbf{h}^{o}) \\ &+ \mathbf{e}_{DC}(\mathbf{r}') \cdot \mathbf{e}_{b}^{DC}(\mathbf{r}' | \delta\mathbf{h}^{o})\end{aligned} \tag{D52}$$

and

$$\gamma_{\mu}^{h}(\mathbf{r}') = \int_{0}^{T} dt'\, \frac{\partial}{\partial t'}\mathbf{h}(\mathbf{r}', t') \cdot \mathbf{h}_{b}(\mathbf{r}', t' | \delta\mathbf{h}^{o}) + \mathbf{h}_{DC}(\mathbf{r}') \cdot \mathbf{h}_{b}^{DC}(\mathbf{r}' | \delta\mathbf{h}^{o}). \tag{D53}$$

In summary, equations (D52) and (D53) are the computational forms of the gradients we are seeking. The back-propagated electric and magnetic fields, $\mathbf{e}_{b}(\mathbf{r}', t' | \delta\mathbf{h}^{o})$ and $\mathbf{h}_{b}(\mathbf{r}', t' | \delta\mathbf{h}^{o})$ are determined from equations (D15) and (D16), where the back-propagated electric field step response, is given by $\mathbf{e}_{b}^{step}(\mathbf{r}', t' | \delta\mathbf{h}^{o}) = \int_{T}^{t'} dt\, \mathbf{e}_{b}(\mathbf{r}', t | \delta\mathbf{h}^{o})$. The DC back-propagated fields, $\mathbf{e}_{b}^{DC}(\mathbf{r}', t' | \delta\mathbf{h}^{o})$ and $\mathbf{h}_{b}^{DC}(\mathbf{r}', t' | \delta\mathbf{h}^{o})$, are determined respectively from equations (D33) and (D49) and (D50). We note that equation (D53) reverts back to the causal form given by Wang et al. (1994) when $\mathbf{h}_{DC}(\mathbf{r}')$ is set to zero. However, this is not the case in equation (D52), when $\mathbf{e}_{DC}(\mathbf{r}')$ is set to zero. In this instance equation (D52) involves a back-propagated electric

field step response, while in Wang et al., (1994), it is incorrectly specified using a back-propagated electric field. Nevertheless, it can be shown that the two types of back-propagated fields are related to each other through a simple time differentiation.

As a final note, equation (D53) requires evaluation of $\mathbf{h}_{DC}(\mathbf{r}')$, which can arise from either inductive or grounded sources. For an inductive source, $\mathbf{h}_{DC}(\mathbf{r}')$ is determined by the impressed source $\mathbf{j}_{imp}$ and variations in μ. Here, $\mathbf{e}_{DC}(\mathbf{r}') = 0$ everywhere. However, if the source is grounded, $\mathbf{h}_{DC}(\mathbf{r}')$ is also influenced by the conduction currents flowing in the earth at steady state because $\mathbf{e}_{DC}(\mathbf{r}') \neq 0$. To separate these two types of responses we consider Ampere's law for two situations:

(1) the magnetic field, $\mathbf{h}_{DC}$ that is influenced by $\mathbf{j}_{imp}$ and variations in μ and σ.

(2) A magnetic field, which we call $\mathbf{h}_{mmr}^{DC}$, that is not influenced by any variation in μ, but is affected by $\mathbf{j}_{imp}$ along with variations in σ.

Thus for case (1)

$$-\sigma\mathbf{e}_{DC} + \nabla \mathrm{x}\mathbf{h}_{DC} = \mathbf{j}_{imp} \tag{D54}$$

and for case (2)

$$-\sigma\mathbf{e}_{DC} + \nabla \mathrm{x}\mathbf{h}_{mmr}^{DC} = \mathbf{j}_{imp}. \tag{D55}$$

Subtracting the two equations produces

$$\nabla \mathrm{x}(\mathbf{h}_{DC} - \mathbf{h}_{mmr}^{DC}) = 0. \tag{D56}$$

Let us define a scattered field

$$\mathbf{h}_s = \mathbf{h}_{DC} - \mathbf{h}_{mmr}^{DC}, \tag{D57}$$

where

$$\mathbf{h}_s = \nabla\psi\,, \tag{D58}$$

on account of equation (D56). We also know that $\nabla\cdot\mu\mathbf{h}_{DC} = 0$ or $\nabla\cdot\mu\mathbf{h}_s = -\nabla\cdot\mu\mathbf{h}_{mmr}^{DC}$. Hence

$$\nabla\cdot\mu\nabla\psi = -\nabla\cdot\mu\mathbf{h}_{mmr}^{DC}\,, \tag{D59}$$

and

$$\mathbf{h}_{DC} = \nabla\psi + \mathbf{h}_{mmr}^{DC}\,. \tag{D60}$$

To complete the solution of $\mathbf{h}_{DC}$ in equation (D60) requires that we specify $\mathbf{h}_{mmr}^{DC}$. This is accomplished by taking the curl of equation (D55) and solving

$$\nabla\mathrm{x}\nabla\mathrm{x}\mathbf{h}_{mmr}^{DC} = \nabla\mathrm{x}\sigma\mathbf{e}_{DC} + \nabla\mathrm{x}\mathbf{j}_{imp}. \tag{D61}$$

Because the DC electric field is curl free, it is determined by applying the divergence operator to equation (D55),

$$\nabla\cdot\sigma\nabla\zeta = -\nabla\cdot\mathbf{j}_{imp}, \tag{D62}$$

where

$$\nabla\zeta = \mathbf{e}_{DC}. \tag{D63}$$

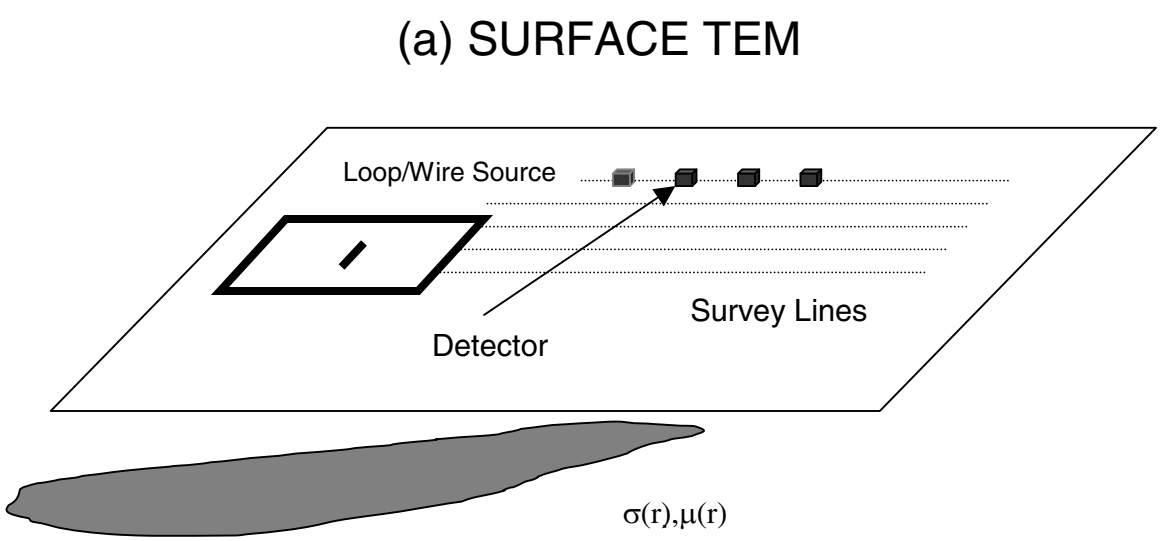
(a) SURFACE TEM
Loop/Wire Source
Survey Lines
Detector
σ(r),μ(r)

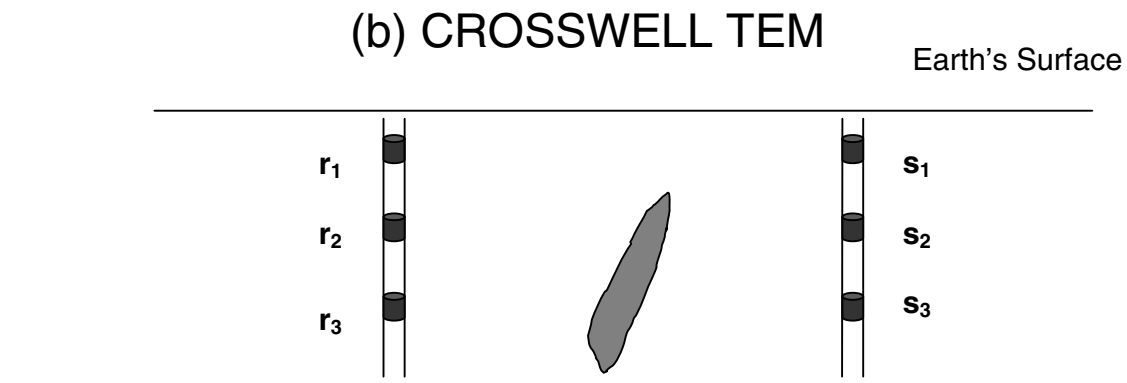
(b) CROSSWELL TEM
Earth's Surface
r1
r2
r3
s1
s2
s3

Figure 1

a) $100*\| \gamma_{\sigma}^{e_y}(r') - {}^{p}\gamma_{\sigma}^{e_y}(r') \| / \| \gamma_{\sigma}^{e_y}(r') \|$.

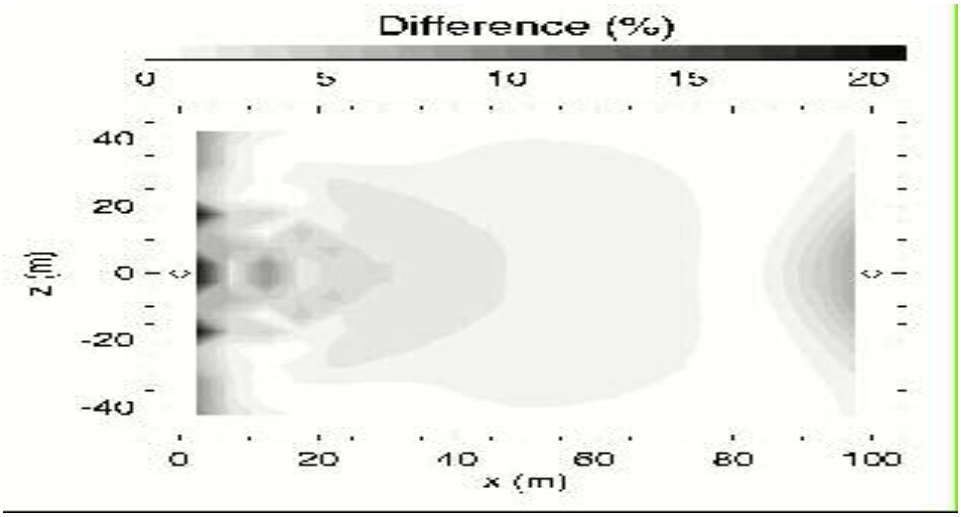

b) $100*\| \gamma_{\sigma}^{u_z}(r') - {}^{p}\gamma_{\sigma}^{u_z}(r') \| / \| \gamma_{\sigma}^{u_z}(r') \|$

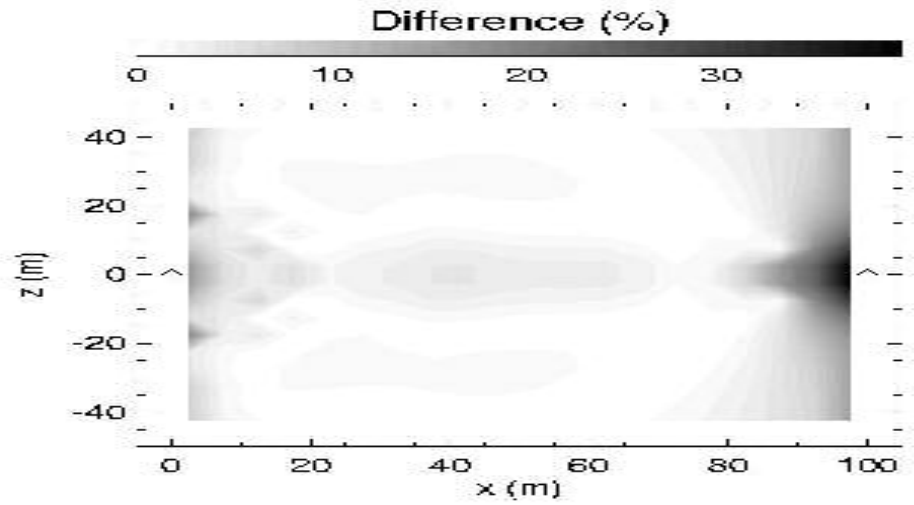

c) $100*\| \gamma_{\sigma}^{h_z}(r') - {}^{p}\gamma_{\sigma}^{h_z}(r') \| / \| \gamma_{\sigma}^{h_z}(r') \|$

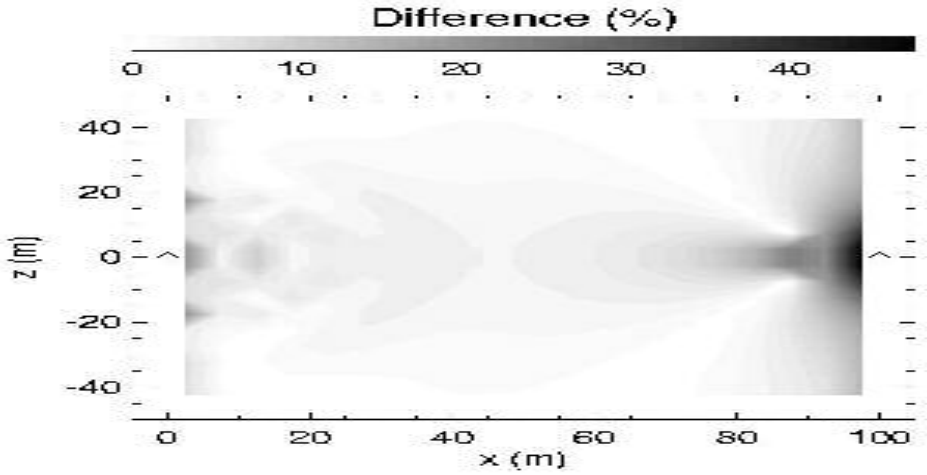

Figure 2

a) $100*\| \gamma_\sigma^{e_y}(r') - {}^{p}\gamma_\sigma^{e_y}(r') \| / \| \gamma_\sigma^{e_y}(r') \|$.

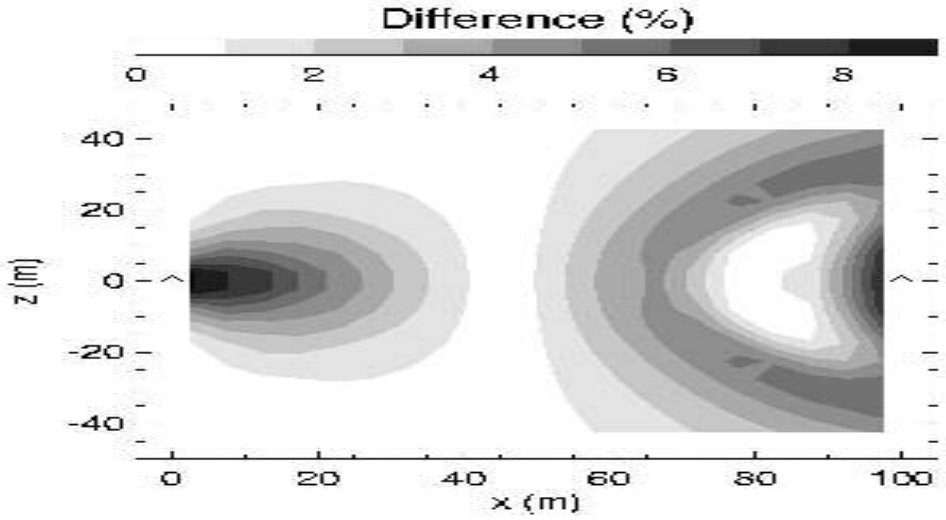

b) $100*\| \gamma_\sigma^{u_z}(r') - {}^{p}\gamma_\sigma^{u_z}(r') \| / \| \gamma_\sigma^{u_z}(r') \|$

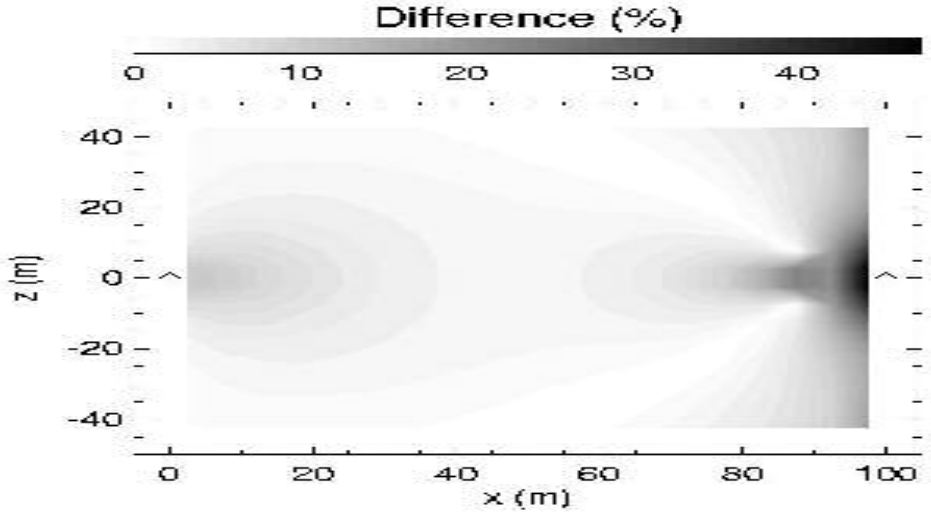

Figure 3

$$100*\| \gamma_{\sigma}^{h_z}(r') - {}^{p}\gamma_{\sigma}^{h_z}(r') \| / \| \gamma_{\sigma}^{h_z}(r') \|$$

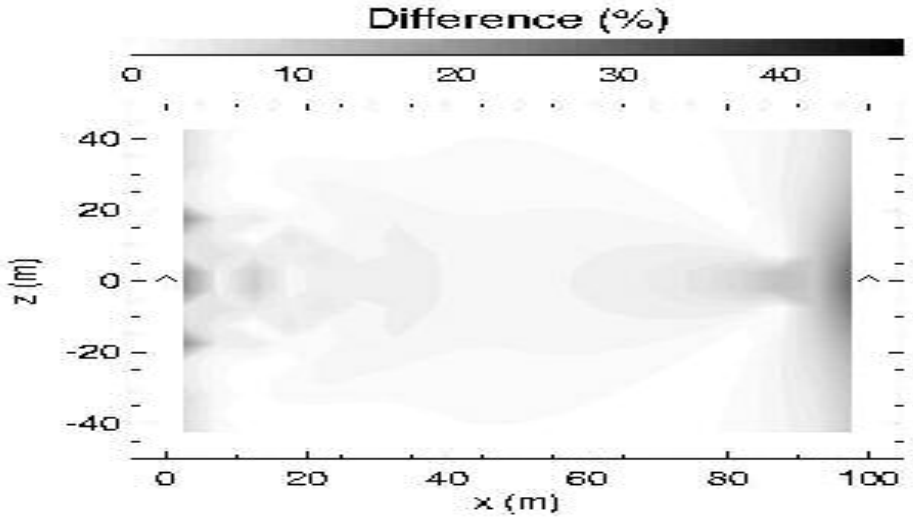

Figure 4

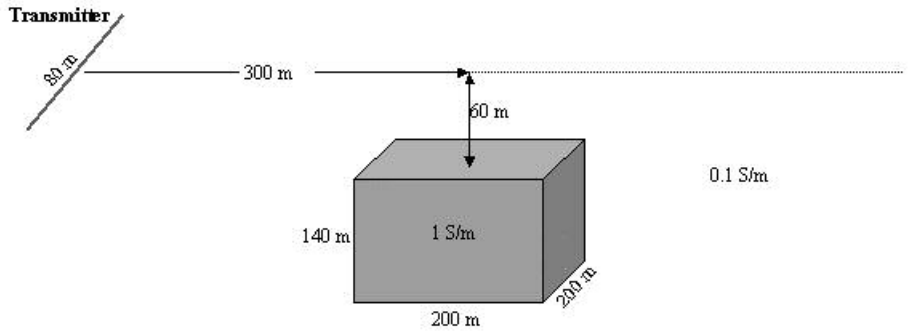

Figure 5

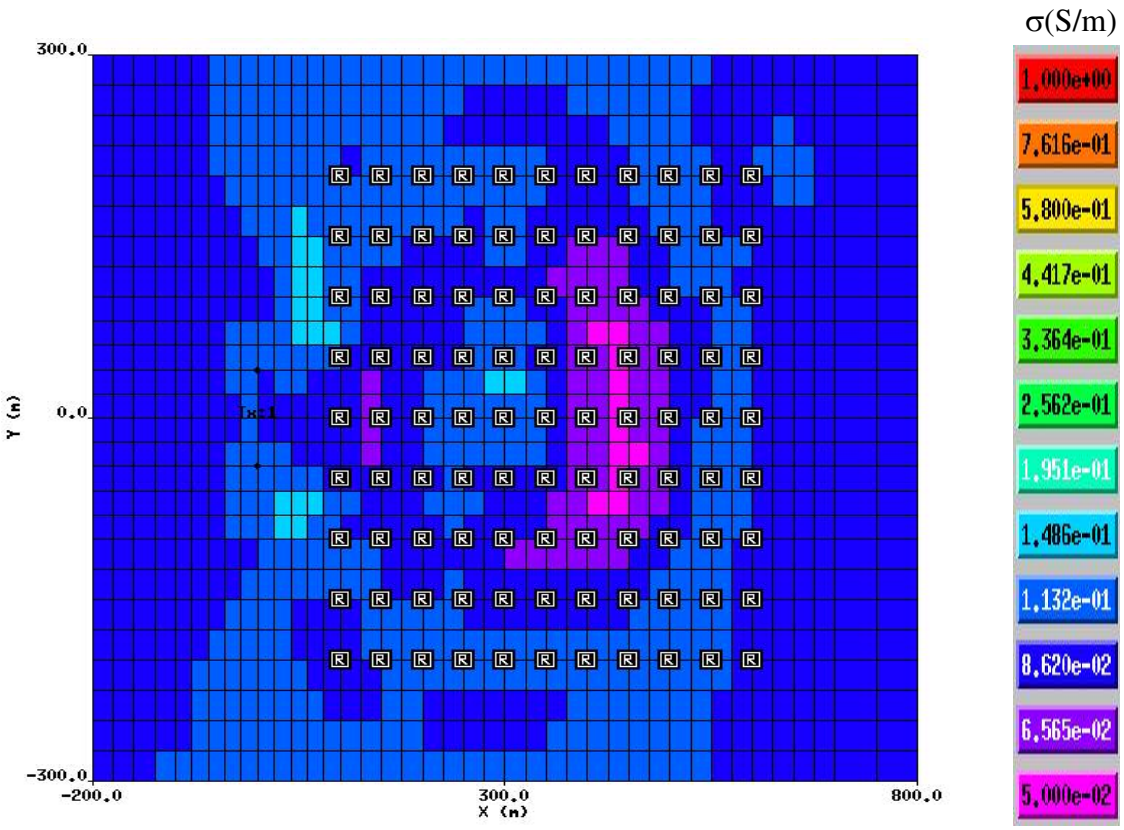
σ(S/m)
1.000e+00
7.616e-01
5.800e-01
4.417e-01
3.364e-01
2.562e-01
1.951e-01
1.486e-01
1.132e-01
8.620e-02
6.565e-02
5.000e-02
300.0
0.0
-300.0
Y (m)
-200.0
300.0
800.0
X (m)

Figure 6

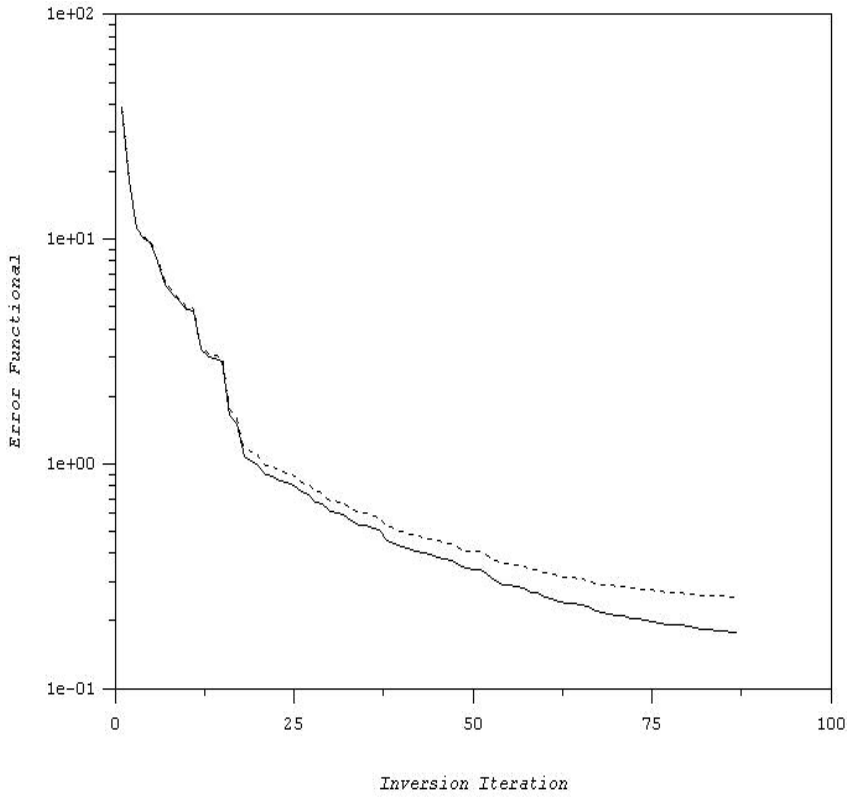
1e+02
1e+01
1e+00
1e-01
Error Functional
0
25
50
75
100
Inversion Iteration

Figure 7

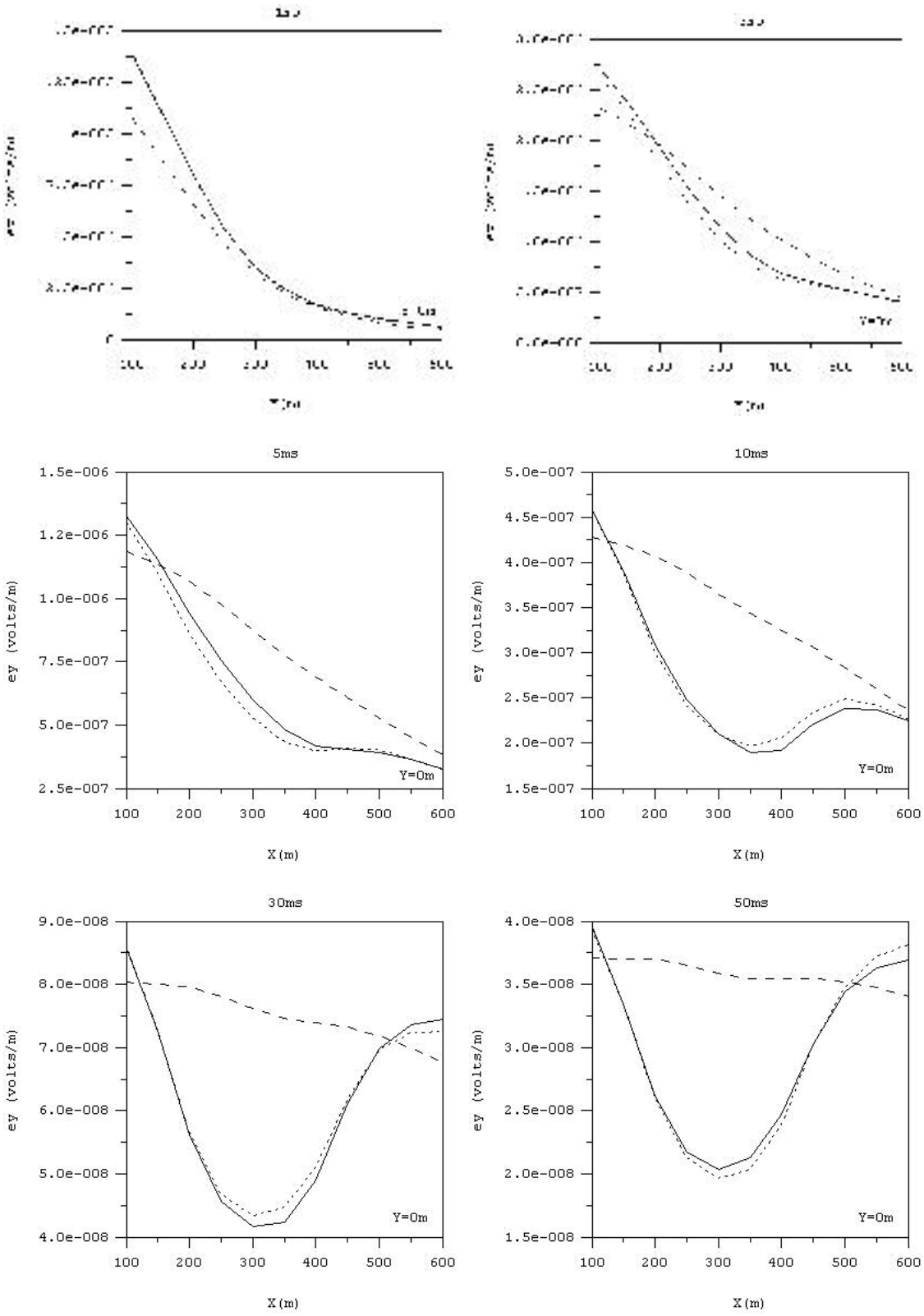

Figure 8

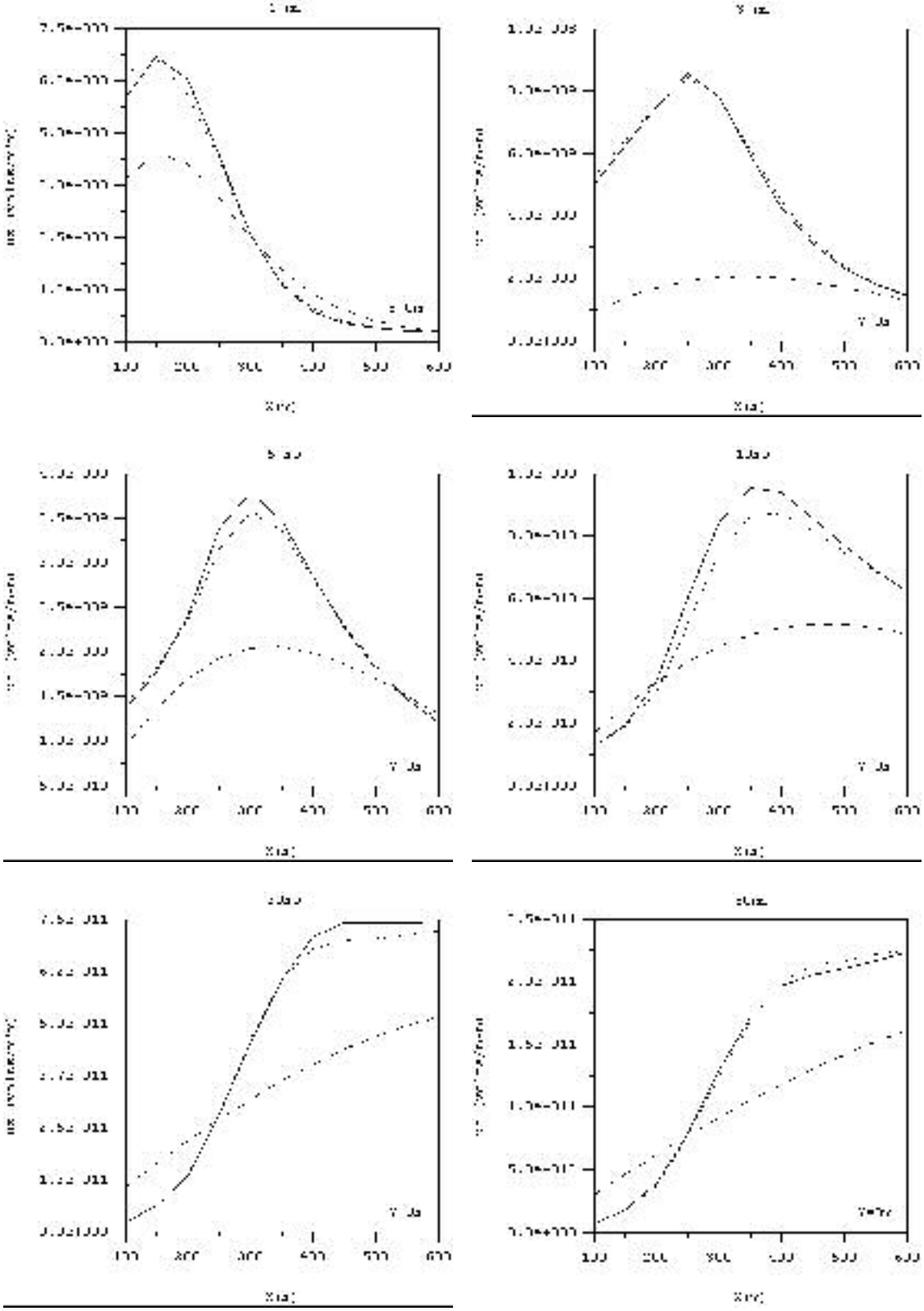

Figure 9

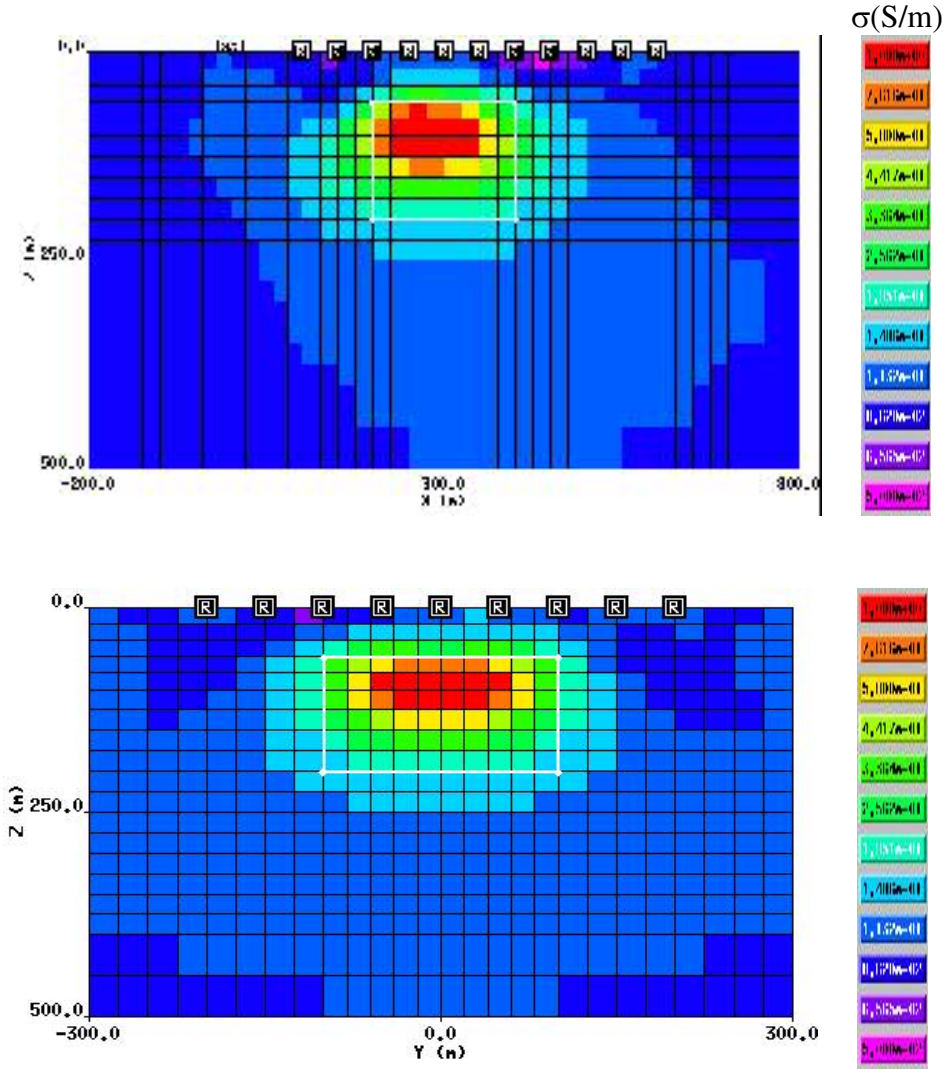

Figure 10

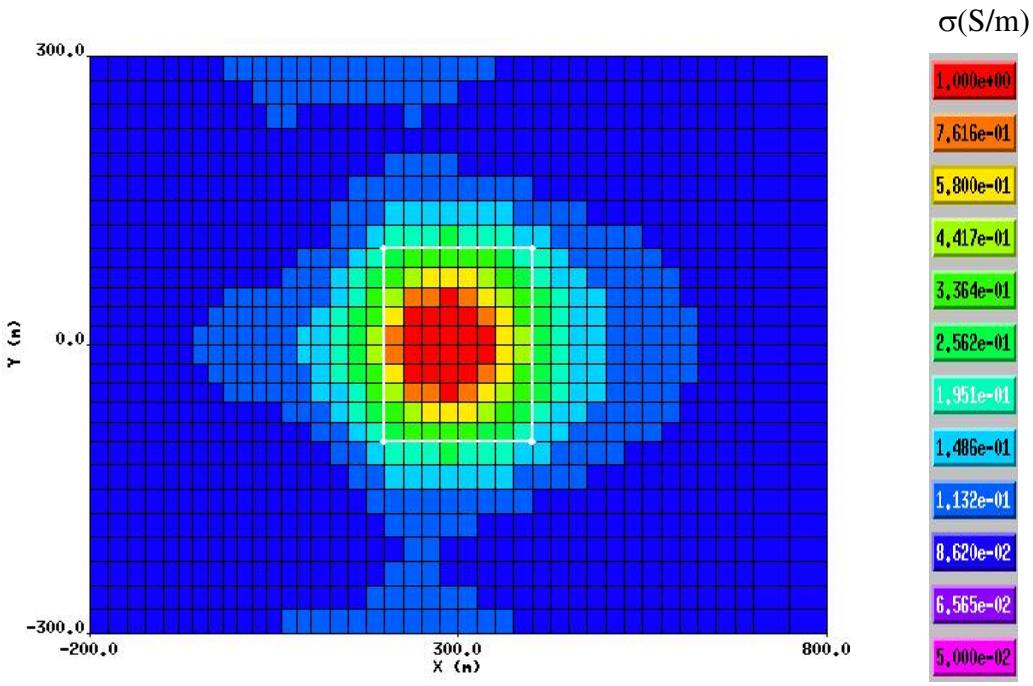
σ(S/m)
300.0
0.0
-300.0
Y (m)
-200.0
300.0
800.0
X (m)
1.000e+00
7.616e-01
5.800e-01
4.417e-01
3.364e-01
2.562e-01
1.951e-01
1.486e-01
1.132e-01
8.620e-02
6.565e-02
5.000e-02

Figure 11

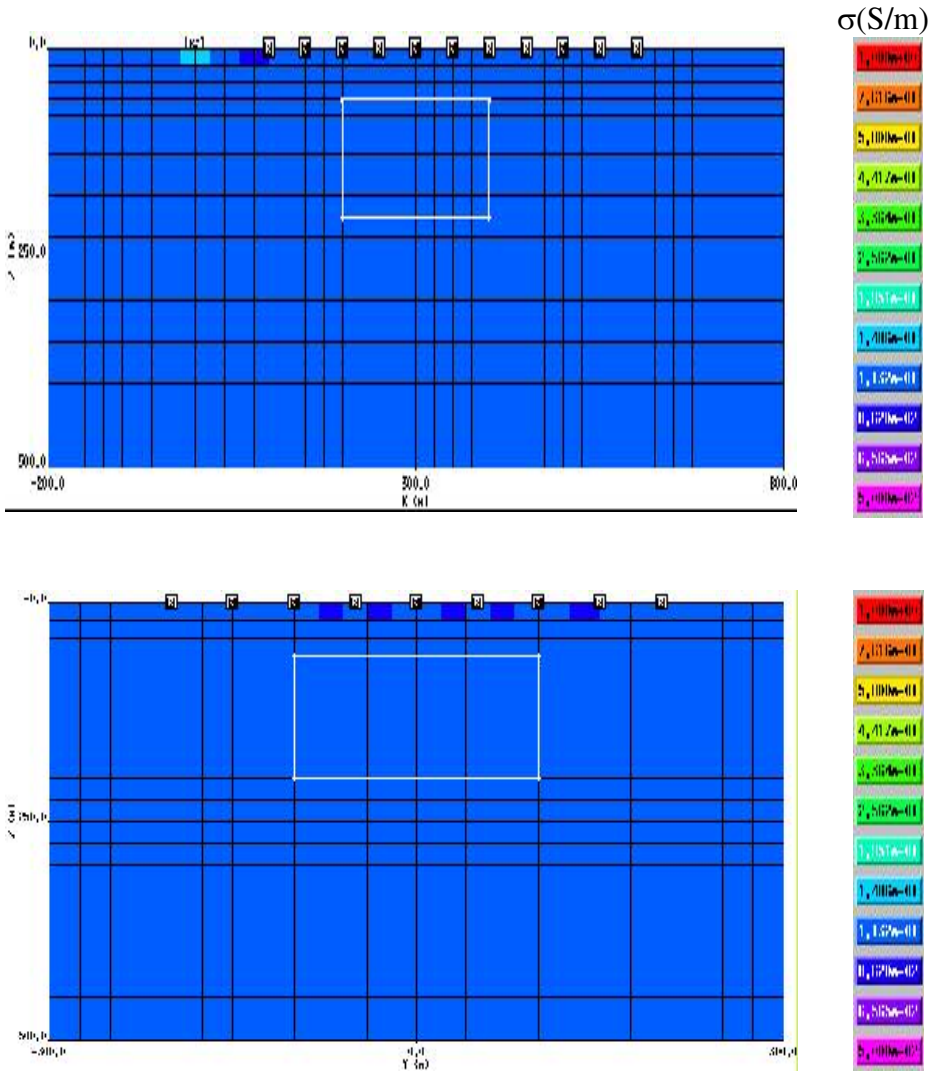

Figure 12

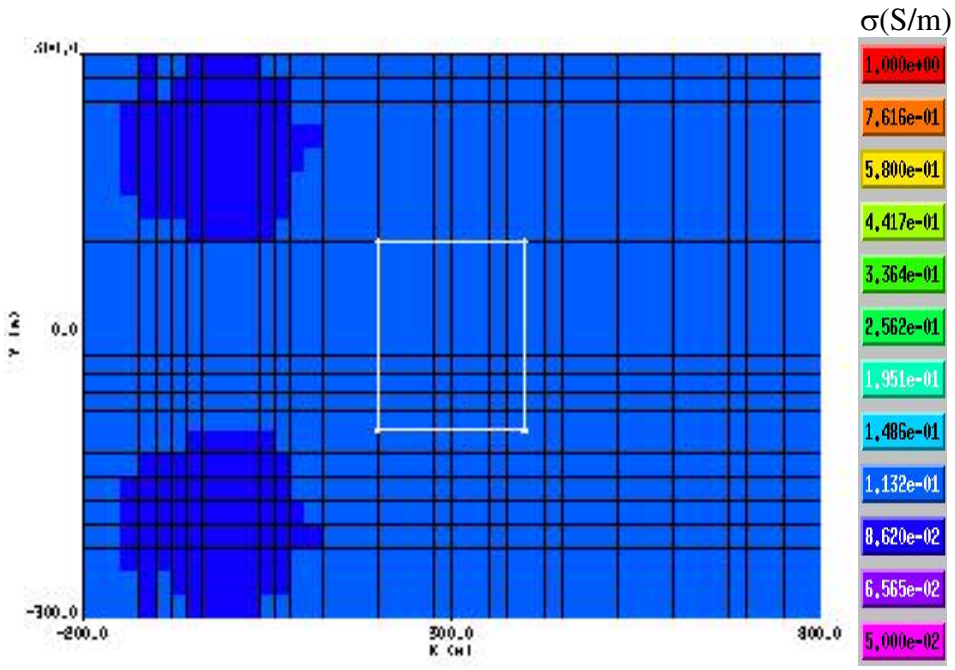
σ(S/m)
1.000e+00
7.616e-01
5.800e-01
4.417e-01
3.364e-01
2.562e-01
1.951e-01
1.486e-01
1.132e-01
8.620e-02
6.565e-02
5.000e-02
0.0
-300.0
-200.0
300.0

Figure 13

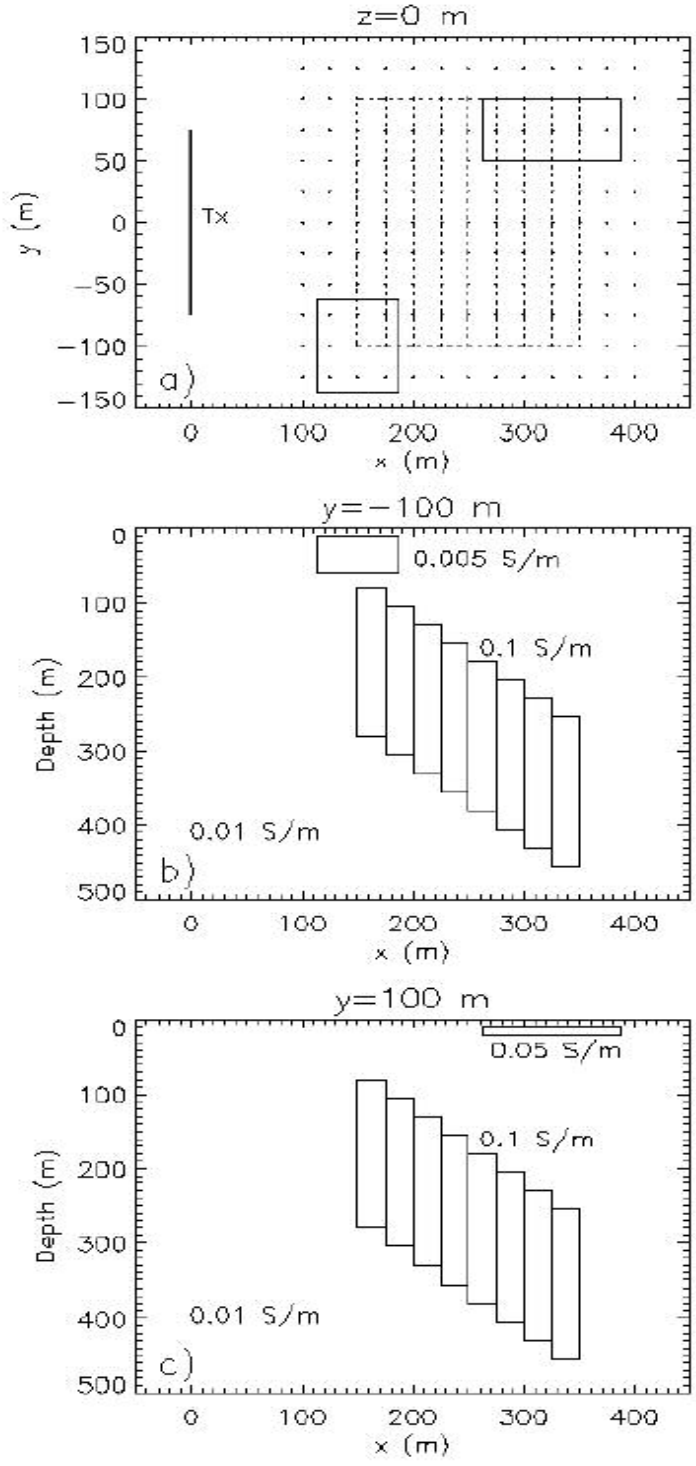
z=0 m
150
100
50
0
−50
−100
−150
y (m)
Tx
a)
0
100
200
300
400
x (m)
y=−100 m
0.005 S/m
0.1 S/m
0.01 S/m
b)
Depth (m)
0
100
200
300
400
500
x (m)
y=100 m
0.05 S/m
0.1 S/m
0.01 S/m
c)
Depth (m)
x (m)

Figure 14

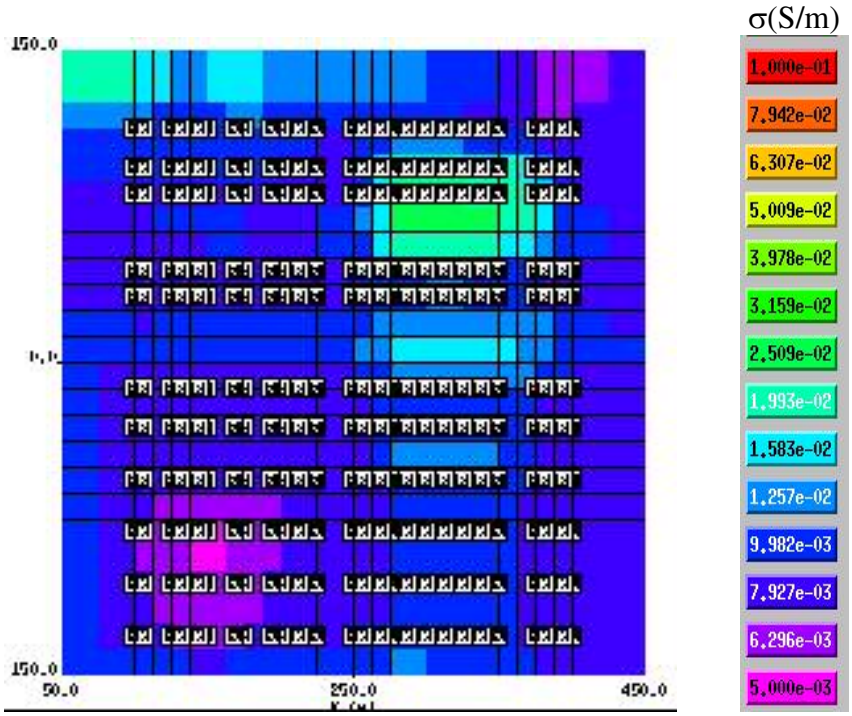
σ(S/m)
1.000e-01
7.942e-02
6.307e-02
5.009e-02
3.978e-02
3.159e-02
2.509e-02
1.993e-02
1.583e-02
1.257e-02
9.982e-03
7.927e-03
6.296e-03
5.000e-03
450.0
50.0

Figure 15

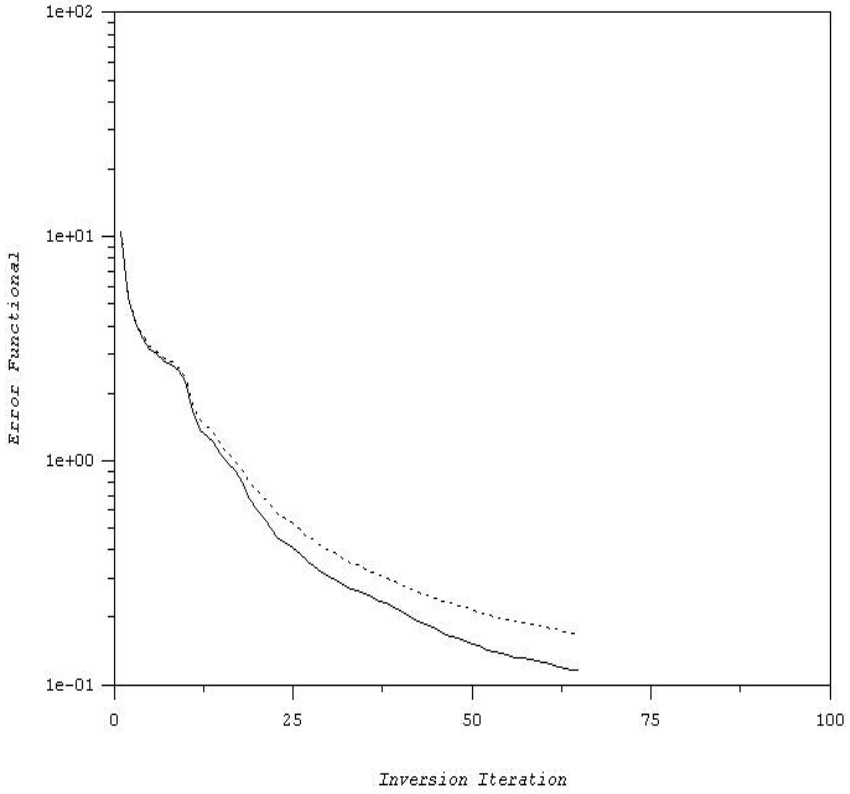
1e+02
1e+01
1e+00
1e-01
Error Functional
0
25
50
75
100
Inversion Iteration

Figure 16

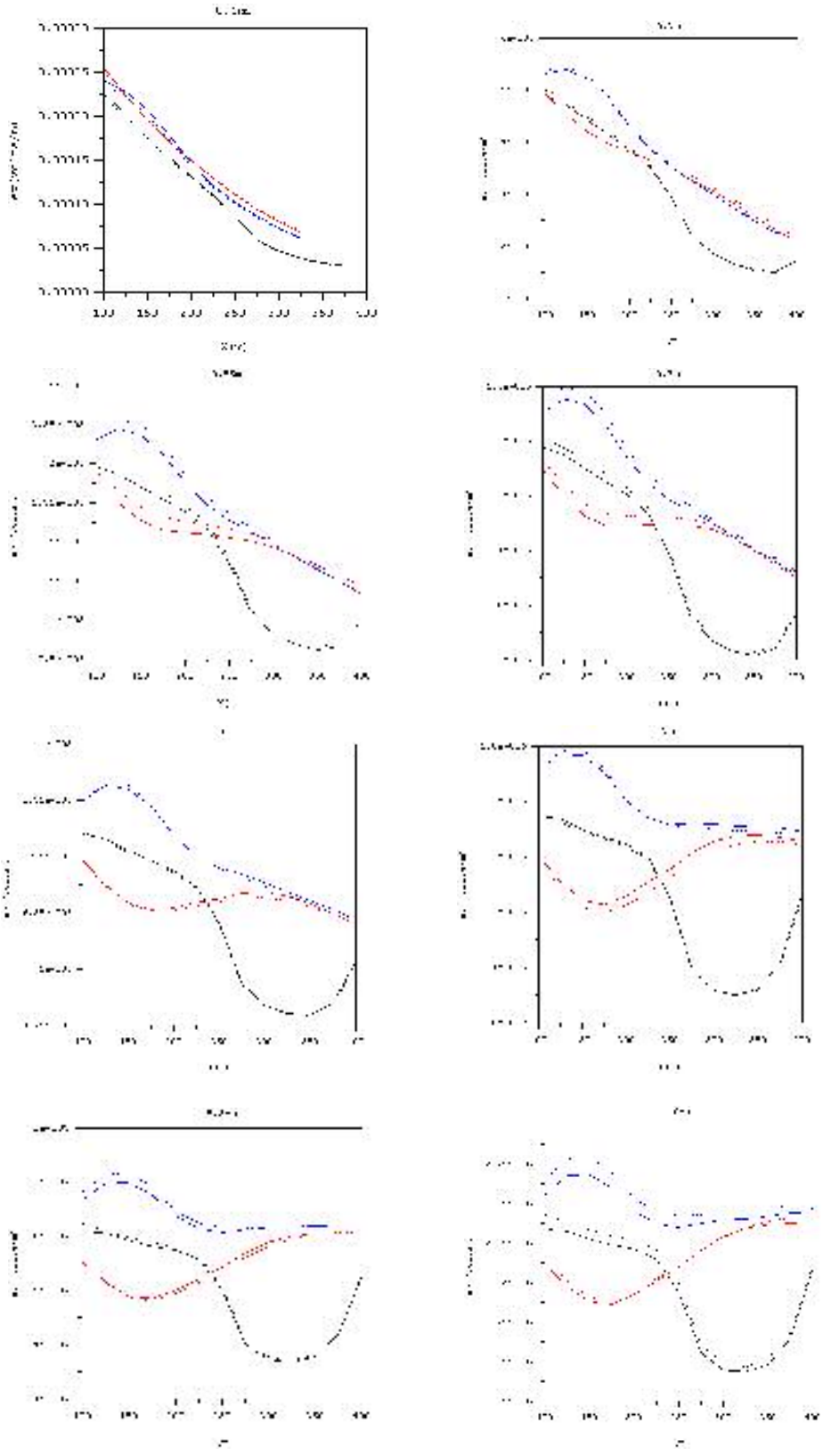

Figure 17

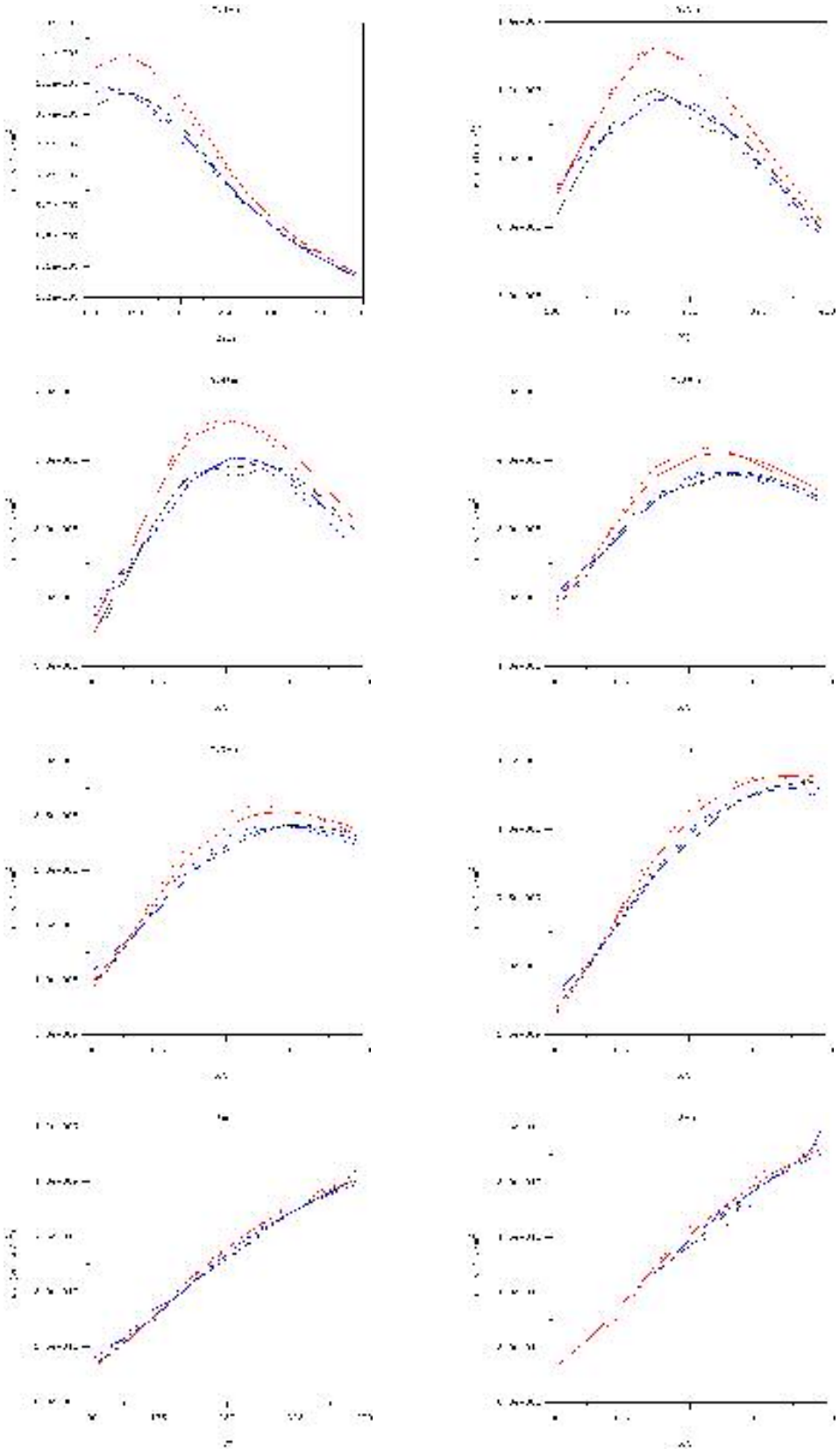

Figure 18

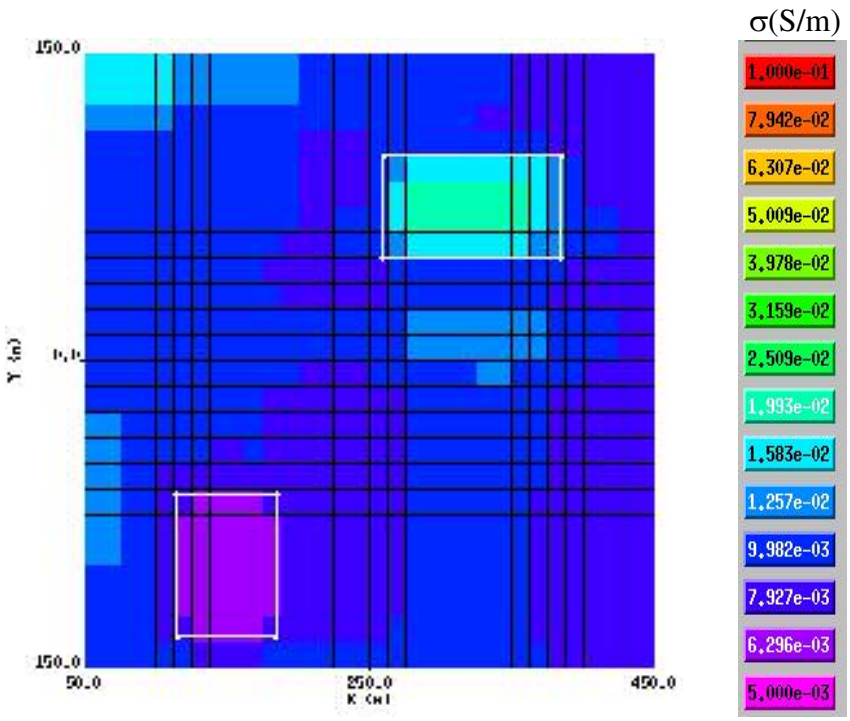
σ(S/m)
1.000e-01
7.942e-02
6.307e-02
5.009e-02
3.978e-02
3.159e-02
2.509e-02
1.993e-02
1.583e-02
1.257e-02
9.982e-03
7.927e-03
6.296e-03
5.000e-03
150.0
50.0
250.0
450.0

Figure 19.

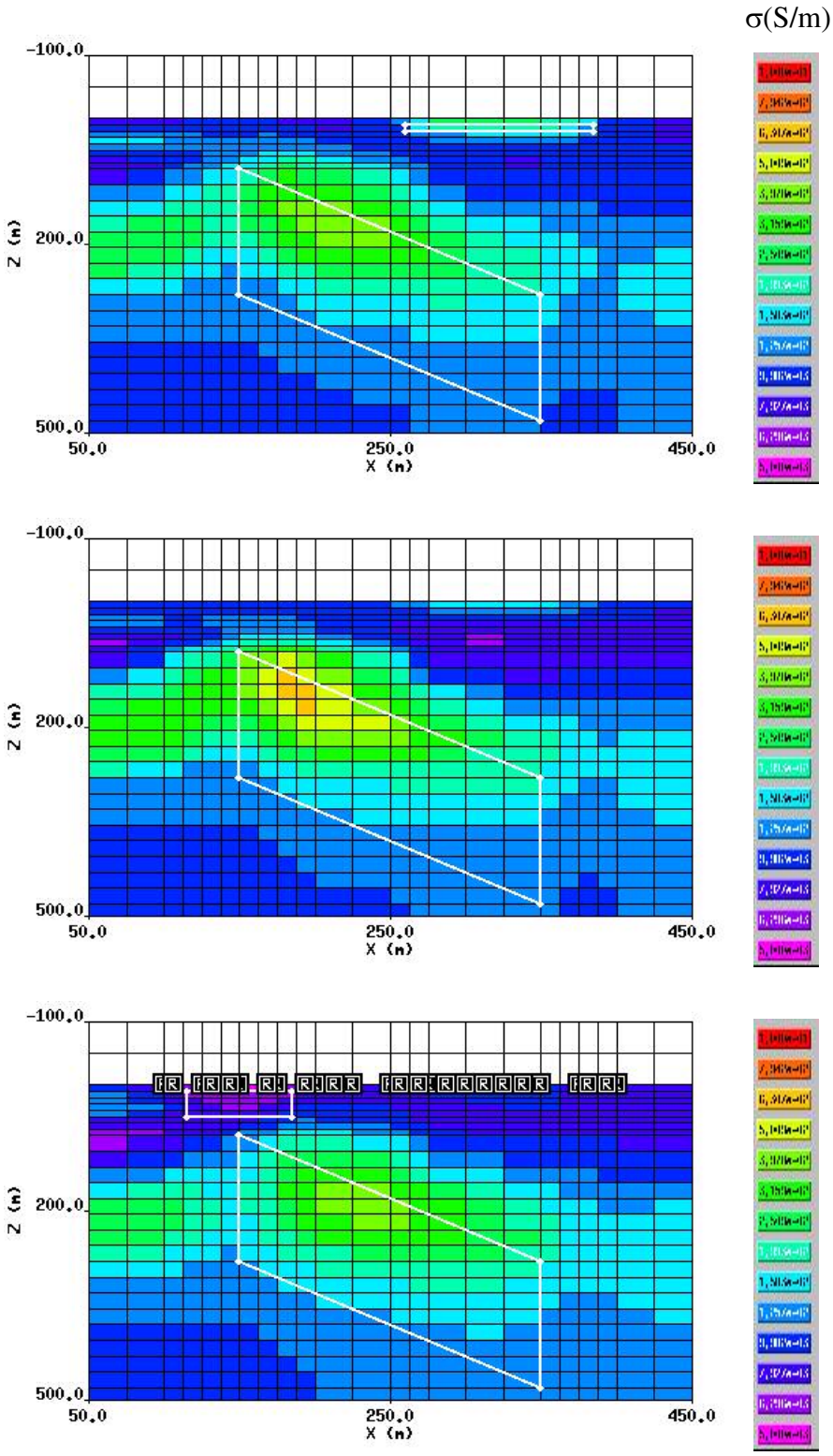

Figure 20